XRD, MÖSSBAUER AND MAGNETIC PROPERTIES OF $CdFe_2O_4$, $Zn_{0.5}(Co, Ni)_{0.5}Fe_2O_4$ AND $Zn_xMn_{1-x}Fe_2O_4$ NANOFERRITES

by

Toitoi Amos Nhlapo

BSc, BSc (Hons) (UFS)

This dissertation is submitted to the University of the Free State in fulfilment of the academic requirements for a Master of Science degree in the Faculty of Natural and Agricultural Sciences, Department of Physics.

May 2012

Supervisor: Dr. J.Z. Msomi

Acknowledgments

I would like to thank the following people for their contributions and sacrifices as indicated bellow towards making this work a success.

- Dr J.Z. Msomi for his supervision, encouragement and guidance throughout the period of this work.

- Dr J.J. Dolo for constant encouragement and support.

- Staff members and my fellow research students in the Department of Physics at the University of Free State (Qwaqwa campus) for their support and encouragement.

My final thanks are reserved for members of my family for their understanding, encouragement and support.

Dedication

I dedicate this work to my family.

Declaration

The candidate wishes to confirm that the work described in this dissertation was carried out by the author in the Department of Physics at University of the Free State. This is original work by the author and has not been submitted in any form to another University or Institution. Credit has been given where use of the work of others is made.

Toitoi Amos Nhlapo

May 2012

Abstract

We report the structural and magnetic properties of $CdFe_2O_4$, $Zn_xMn_{1-x}Fe_2O_4$ ($0 \leq x \leq 1.0$) and $Zn_{0.5}(Co,\ Ni)_{0.5}Fe_2O_4$ oxides. The bulk $CdFe_2O_4$ ferrite was synthesized by solid state reaction. Upon high energy ball milling, the fine powders with particle size of about 10 nm were produced. The structural and magnetic changes as induced by high energy ball milling have been investigated. The $Zn_xMn_{1-x}Fe_2O_4$ and $Zn_{0.5}(Co,\ Ni)_{0.5}Fe_2O_4$ nanosized oxides with particle size between 5 nm and 14 nm were also produced by glycolthermal reaction under low reaction temperature of 200 ^{0}C. The compounds were characterized by X–ray diffraction (XRD), Mössbauer spectroscopy at 300 K, vibrating sample magnetometer (VSM) and superconducting quantum interference device (SQUID) from 2 K to 400 K measurements.

XRD data confirm formation of pure cubic spinel phase in all the $CdFe_2O_4$ oxide samples. A general decrease in lattice constant of $CdFe_2O_4$ oxide with increasing milling time has been observed. This is associated with structural disorder induced by milling. The Mössbauer spectra indicate paramagnetic spin state in all the $CdFe_2O_4$ samples. An increase in magnetization with increasing milling time (reducing particle size) occurs. This can be explained by the redistribution of Cd ions in both tetrahedral (A) and octahedral (B) sites. The coercive fields of the milled $CdFe_2O_4$ oxide appear to be more sensitive to measuring temperature compared to the unmilled sample. For the 50 hours milled sample coercive fields increase from about 9 Oe at 300 K to 520 Oe at 10 K. A smaller increase in coercive fields from 9 Oe at 300 K to 200 Oe at 10 K occurs in the unmilled oxide. The variation of magnetization as a function of measuring temperature is also presented. An anomalous variation of field cooled magnetization as a function of temperature in the 50 h milled $CdFe_2O_4$ has been observed.

The $Zn_{0.5}(Co,\ Ni)_{0.5}Fe_2O_4$ and $Zn_xMn_{1-x}Fe_2O_4$ compounds crystallized with single phase cubic spinel structure. The properties of Zn–Ni and Zn–Co samples

are closely related. The variation of Zn concentration has significant effects on the structural and magnetic properties of $Zn_xMn_{1-x}Fe_2O_4$ compounds. A non–linear variation of the size of the unit cell with increasing Zn content occurs. The ^{57}Fe Mössbauer spectra show paramagnetic spin states in all Zn–Mn compounds. We have found a discontinuity in the temperature dependence of magnetization of $Zn_{0.4}Mn_{0.6}Fe_2O_4$ which suggests more than one magnetic phase in both as–prepared and annealed samples.

Publications based on the current work

- J.Z. Msomi, T.A. Nhlapo, T. Moyo, M. Öztürk, N. Akdoğan; Structural and magnetic changes induced by high energy ball milling in $CdFe_2O_4$ oxide, Journal of Super Cond. Nov. (submitted for publications, May 2012).

- J.Z. Msomi, T.A. Nhlapo, T. Moyo, J. Snyman, A.M. Strydom; Structural, Mössbauer and magnetic properties of $Zn_xMn_{1-x}Fe_2O_4$ nanoferrites, Journal of Super Cond. Nov. (submitted for publications, May 2012).

Contents

1 Introduction to ferrites **1**

1.1 Crystal structure of ferrites 1

1.2 Synthesis of ferrites 3

1.3 Magnetic properties of ferrites 4

1.4 Applications of ferrites 5

1.5 Motivation for current work 6

2 Basic principles of Mössbauer spectroscopy **9**

2.1 Mössbauer effect 9

2.2 Recoil–free fraction 12

2.3 Hyperfine interactions 12

2.3.1 Isomer shift 13

2.3.2 Electric quadrupole splitting 15

2.3.3 Magnetic splitting 15

3 Experimental details **18**

3.1 Sample preparation 18

3.1.1 Solid state reaction 18

3.1.2 High energy ball milling 19

3.1.3 Glycolthermal reaction 19

3.2 Mössbauer measurements 20

3.3 Magnetization measurements 22

3.4 X–ray diffraction 24

4 Magnetic properties of bulk and nanosized $CdFe_2O_4$ oxides **27**

4.1 X-ray diffraction results 27

4.2 Mössbauer spectroscopy results 32

4.3 Magnetization results 35

4.4 Conclusions 40

5 Magnetic properties of $Zn_{0.5}(Ni, Co)_{0.5}Fe_2O_4$ and $Zn_xMn_{1-x}Fe_2O_4$ oxides **42**

5.1 X–Ray diffraction results 43

5.2 Mössbauer spectroscopy results 49

5.3 Magnetization measurements 52

5.4 Conclusions 59

6 Conclusions **60**

Bibliography **61**

List of Figures

1.1 The occupation of tetrahedral (A) and octahedral (B) sites in a spinel structure [2]. 2

1.2 The magnetic order in a (a) ferromagnet (b) antiferromagnet (c) ferrimagnet and (d) paramagnet. 5

2.1 Resonant overlap in free atoms [45]. 11

2.2 (a) Isomer shift, (b) Isomer shift and quadrupole splitting [43]. . 14

2.3 Magnetic splitting in ^{57}Fe nucleus [43]. 17

3.1 Nuclear Decay scheme of ^{57}Co [45]. 21

3.2 Experimental set–up for the Mössbauer spectrometer. 23

3.3 Generation of x–rays [47]. 26

4.1 Variation of XRD patterns for $CdFe_2O_4$ with milling time. . . . 28

4.2 Variation of grain size for $CdFe_2O_4$ with milling time. 31

4.3 Variation of Mössbauer spectra for $CdFe_2O_4$ as a function of milling time. 33

4.4 Variation of magnetization curves for $CdFe_2O_4$ oxides with milling time at 300 K, as prepared and 50h milling time respectively. . . 36

4.5 Variation of coercive fields as a function of temperature for as prepared (0 h) and 50 h milled $CdFe_2O_4$ oxides. 38

4.6 Variation of coercive fields as a function of $T^{1/2}$ for (0 h) and 50 h milled $CdFe_2O_4$ oxides. 39

4.7 Variation of magnetization as a function of temperature for the (a) as–prepared (0 h) and (b) 50 hours milled samples. 41

5.1 Variation of XRD patterns for $Zn_{0.5}(Ni, Co)_{0.5}Fe_2O_4$ oxides. . . 44

5.2 Variation of XRD patterns for $Zn_xMn_{1-x}Fe_2O_4$ with x. 45

5.3 Variation of XRD spectra for $Zn_{0.4}Mn_{0.6}Fe_2O_4$ (annealed at 600 ^{0}C) with annealing time. 47

5.4 Variation of lattice parameter for $Zn_xMn_{1-x}Fe_2O_4$ oxides as a function of x. 48

5.5 Variation of Mössbauer spectra for $Zn_xMn_{1-x}Fe_2O_4$ as a function of x. 50

5.6 Variation of magnetization curves for (a) $Zn_{0.5}Ni_{0.5}Fe_2O_4$ ans (b) $Zn_{0.5}Co_{0.5}Fe_2O_4$ oxides with measuring temperature. 54

5.7 Variation of coercive fields for $Zn_{0.5}(Ni, Co)_{0.5}Fe_2O_4$ oxides with measuring temperature. 55

5.8 Variation of magnetization as a function of temperature for $Zn_{0.5}(Ni, Co)_{0.5}Fe_2O_4$ oxides. 56

5.9 Variation of magnetization as a function of temperature for (a) raw and (b) annealed $Zn_{0.4}Mn_{0.6}Fe_2O_4$ oxides. 57

5.10 The hysteresis loop for raw $Zn_{0.4}Mn_{0.6}Fe_2O_4$ oxide. 58

List of Tables

4.1 Variation of grain size (D), lattice parameter (a) and x–ray density (ρ_X) with milling time. 30

4.2 Variation of isomer shift (δ), quadrupole splitting (ε), line width (l) and Fe^{3+} fraction (f) on A and B sites for $CdFe_2O_4$ oxide with milling time. 34

4.3 Variation of coercive field (H_c), saturation (M_S) and remanent (M_R) magnetization with measuring temperature (T) for $CdFe_2O_4$ oxides. 37

5.1 Variation of grain size (D), lattice parameter (a) and x–ray density (ρ_X) for $Zn_xMn_{1-x}Fe_2O_4$ as a function of x. 46

5.2 Variation of grain size (D), lattice parameter (a) and x-ray density (ρ_X) with annealing time (t) for $Zn_{0.4}Mn_{0.6}Fe_2O_4$ oxides annealed at 600 ^{0}C. 49

5.3 Variation of isomer shift (δ), quadrupole splitting (ε), line width (l) and Fe fraction (f) at A and B sites of $Zn_xMn_{1-x}Fe_2O_4$ as a function of x. 51

Chapter 1

Introduction to ferrites

Ferrites are oxides with the chemical formula MFe_2O_4. M is a divalent metal ion such as Co^{2+}, Mn^{2+}, Cu^{2+}, Zn^{2+}, Mg^{2+} etc. [1]. In mixed ferrites M is a mixture of these ions. There are usually two types of ferrites, namely, soft and hard ferrites. Soft ferrites exhibit cubic spinel structure and hard ferrites have hexagonal crystal structure. In this work the structural and magnetic study of soft ferrites is presented. This chapter gives a brief description of the spinel crystal structure, synthesis, magnetic properties and applications of ferrites. The motivation for the current work is also given.

1.1 Crystal structure of ferrites

The crystal structure of ferrite materials is that of a mineral spinel with composition $MgAl_2O_4$ shown in Figure 1.1. In ferrites Mg and Al ions are replaced by divalent metal and Fe ions respectively. The spinel lattice consists of a cubic closed–packed array of oxygen ions with two interstitial positions called A and B sites. The A sites are surrounded by four oxygen ions forming tetrahedral symmetry and the B sites are surrounded by six oxygen ions forming an octahedron. The tetrahedral (A) and octahedral (B) sites are occupied by metal cations. The chemical formula for ferrites is sometimes written as AB_2O_4. Various ions can be placed at either A or B sites. In a normal spinel

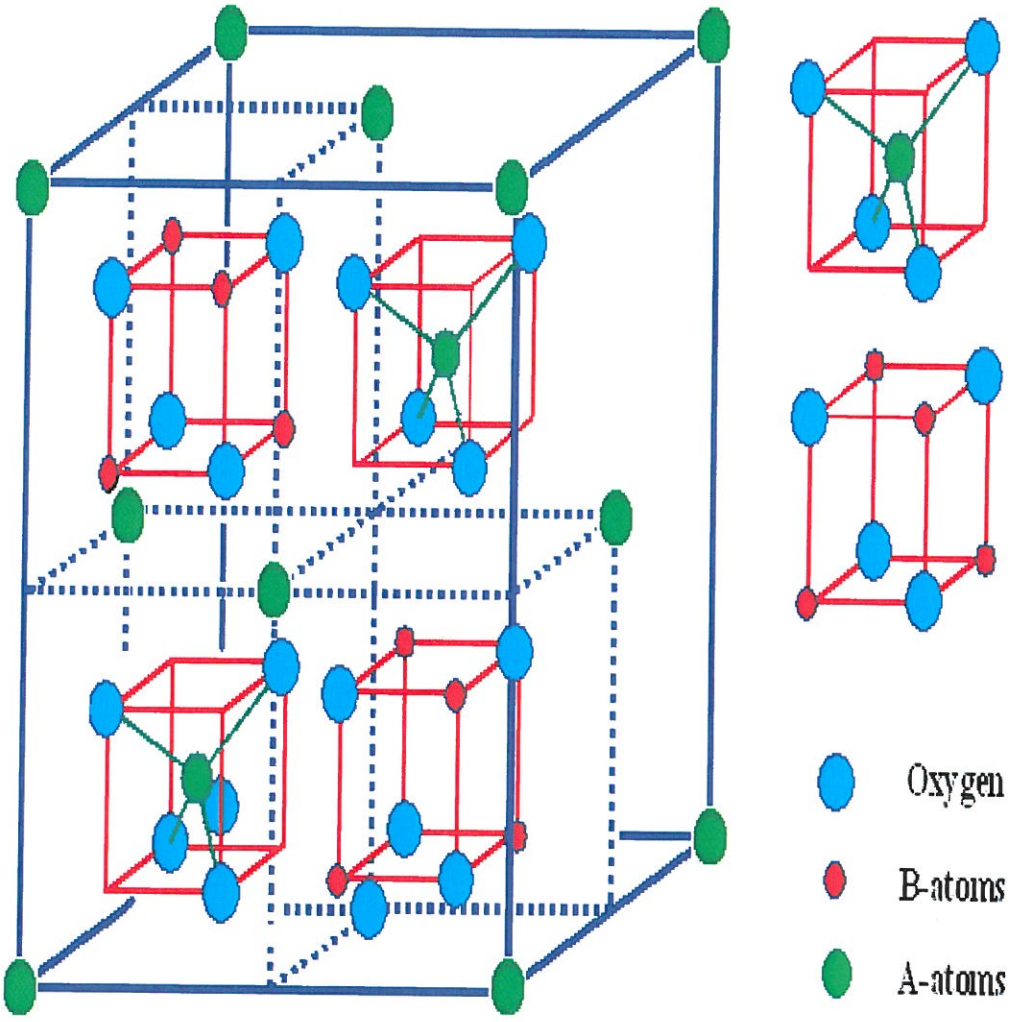

Figure 1.1: The occupation of tetrahedral (A) and octahedral (B) sites in a spinel structure [2].

all the divalent metal cations occupy A sites and the trivalent Fe ions occupy B sites. The inverse spinel has divalent ions occupying B sites and trivalent Fe ions equally distributed between A and B sites. The zinc ferrite, $ZnFe_2O_4$, is a normal spinel with all Zn^{2+} and Fe^{3+} ions occupying A and B sites respectively [3]. The $NiFe_2O_4$ ferrite is an example of an inverse spinel where all Ni^{2+} ions occupy B sites and Fe^{3+} ions are distributed equally between A and B sites [4–6].

1.2 Synthesis of ferrites

Bulk ferrite materials are generally produced by solid state reaction [7–10]. The starting materials are high purity oxides. The procedure involves two sample preparation stages of high temperature heat treatments. This technique is therefore generally called double sintering method. The initial pellets are heat treated at about 950 ^{0}C. The products are reground and pressed to final pellets which are annealed at a higher temperature. Sometimes samples are heated in sealed quartz tubes and degassed under vacuum. This allows pellets to be quenched in liquid nitrogen immediately after heat treatment in order to preserve the phase that occurs at high temperature.

Ferrites materials can also be prepared by high energy ball milling [11–16]. Materials with controlled particle size can be produced with this technique. The starting pre–calculated stoichiometric oxides are loaded with hardened steel balls into hardened steel vials. The influence of milling conditions on properties is discussed in reference [17]. Ferrites in bulk quantities for commercial use can be easily produced by high energy ball milling.

Various chemical methods such as hydrothermal [18, 19], co–precipitation [4, 20–22], sol–gel [23, 24], forced hydrolysis [25], citrate precursor [26, 27] and low temperature solid state reaction [5] have appeared in the literature recently. These methods are being developed for synthesis of ferrites with fine particles. During hydrothermal or co–precipitation method chlorides, nitrates

or sulphates are used as starting materials. The precipitate is formed by addition of a base like NaOH. After washing, the precipitate is reacted in a pressure reactor by boiling in deionozed water for at least 3 hours.

1.3 Magnetic properties of ferrites

The magnetic behaviour in ferrites is similar to that of a ferromagnet where magnetic moments are aligned parallel to each other as shown in Figure 1.2 (a). As the sample measuring temperature is decreased below the Curie temperature, the magnetization rapidly increase at first and then slowly rises to a maximum at absolute zero. The magnetic properties are also characterized by a non–linear variation of the magnetization with an applied magnetic field. When the temperature is increased above the Curie point a disordered spin state occurs (see Figure 1.2 (d)). This can be seen by the onset of zero magnetization during magnetization measurements or collapse of a six line Mössbauer spectrum to a doublet during Mössbauer experiment.

The magnetism in ferrites is ferromagnetism. The spin orientations are similar to antiferromagnetic alignment of magnetic moments as shown in Figure 1.2 (b). This is due to negative exchange interactions between magnetic moments. The anti–parallel alignment of magnetic moments results in zero spontaneous magnetization for antiferromagnets. In the case of ferrites, the magnetic moments on the adjacent sublattices are unequal and anti–parallel as shown in Figure 1.2 (c). There is therefore a resultant magnetization due to the difference in the magnitude of the magnetic moments. Ferrimagnetism is described using a two sublattice model [28].

The interactions between neighbouring magnetic ions in ferrites occurs via an intervening oxygen ion. The superexchange interactions between magnetic ions at A or B sites (intrasublattice interactions) are characterized by exchange integrals J_{AA} (A–O–A) or J_{BB} (B–O–B). The intersublattice interactions between A and B sites magnetic moments are characterized by exchange integrals

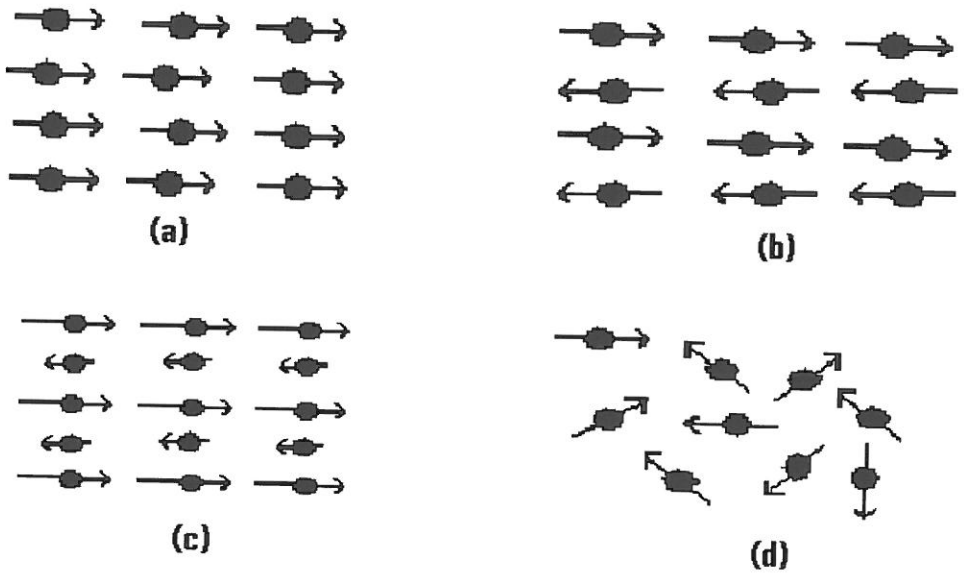

Figure 1.2: The magnetic order in a (a) ferromagnet (b) antiferromagnet (c) ferrimagnet and (d) paramagnet.

J_{AB} (A–O–B) [29]. The intrasublattice interactions tend to align magnetic moments ferromagnetically. The exchange interactions between A and B sites magnetic moments (intersublattice) are negative and therefore tend to align the A and B sublattices antiferromagnetically [30]. There is usually a competition between intersublattice and intrasublattice interactions. Ferrimagnetic ordering takes place when the intersublattice interactions are stronger than the intrasublattice interactions [29].

1.4 Applications of ferrites

Ferrites have a wide range of applications in the electronic industry and medicine. Intrinsic robustness, high negative magnetoelastic behavior and ability to work at high frequencies make cobalt ferrite ($CoFe_2O_4$) suitable for the development of magnetostrictive materials [31]. In modern technology the magnetic nanoparticles have great potential for biomedical applications such as improv-

ing the quality of magnetic resonance imaging (MRI), hyperthermic treatment for malignant cells, site specific drug delivery and manipulating cell membranes [32]. Magnetite is an important member of ferrites. It is used in efficient hyperthermia for cancer MRI contrast agents [22]. The nano–sized $CoFe_2O_4$ oxide have high coercive field and moderate saturation magnetization. These properties combined with physical and chemical stability make $CoFe_2O_4$ nanoparticles suitable for magnetic recording applications such as audio, video tape and high density recording disks [55]. For such applications it is important to produce stable single domain particles [34]. Mn–Zn ferrites have high magnetic permeability, saturation magnetization, dielectric resistivity and relatively low eddy current losses. These properties make them suitable for applications in transformers, magnetic recording heads, noise filters, electromagnetic gadgets, information storage systems, medical diagnostic devices, magnetic refrigeration, magnetic fluids, microwave devices, computer memory chips, fabrication of radio frequency coils and rod antennas. They are also used in biomedicine as magnetic carriers, such as bio–separation, enzyme and protein immobilization [35–37].

1.5 Motivation for current work

The magnetic properties of ferrites can be controlled by suitable substitution at A and B sites [37]. Manganese ferrite, $MnFe_2O_4$ is an inverse spinel with Fe^{3+} ions distributed equally between A and B sites. Dilution by nonmagnetic divalent ions such as Zn^{2+} ions at A site reduces the amount of magnetic Fe ions. This usually results in an increase in magnetization. Making suitable substitution can tune the magnetic properties. Depending on type of cations at A and B sites, ferrimagnetic, antiferromagnetic and paramagnetic behavior can be observed in ferrites [37]. Ferrites with similar composition produced from different laboratories have sometimes been found to have different magnetic properties. This may be due to differences in particle size or distribution of

cations between A and B sites. The synthesis technique is therefore expected to have significant effect on the properties [20].

The properties of nanosized magnetic particles are also different from the corresponding bulk counterpart. This has aroused increasing interest among researchers. A unique feature of magnetic nano–particles is superparamagnetism. In this magnetic state there is weak interparticle magnetic interactions. Each nanoparticle has well defined magnetic order and behaves like a paramagnetic atom with large magnetic moments which act independently [32, 38]. Super spin–glass behaviour can be observed where there is sufficiently strong interparticle magnetic interaction and the ensemble of nanoparticle can show a collective behavior [32]. Superparamagnetic behavior can be seen from measurements of magnetization as a function of external magnetic field and temperature. The very low values in coercive fields and remanence of the hysteresis loop indicate superparamagnetic behavior. The collapse of the six line Mössbauer spectra into a doublet also marks the onset of paramagnetism. Superparamagnetic nanoparticles are relevant in important modern technologies such as magnetic resonance imaging contrast agents, ferrofluids and magnetocarolic refrigeration [38]. Nano–crystalline Mn–Zn have been the subject of intense research [11–13, 18–20, 22, 36, 37, 40–42]. These compounds have wide applications in industry as discussed in section 1.4. Hense any systematic study of ferrite compounds is important. The main objectives of the current work is to undertake (carry–out) a systematic study of the magnetic properties of ferrites in order to:

- investigate the effects of grain size reduction on the properties and
- superparamagnetic behaviour in nanoferrites.

In this work we have produced bulk $CdFe_2O_4$ oxide by solid state reaction and systematically reduced particles to nanometer scale by using high energy ball milling. The $Zn_{0.5}Co_{0.5}Fe_2O_4$ and $Zn_xMn_{1-x}Fe_2O_4$ mixed ferrites with fine particles have been produced by glycolthermal reaction under low reac-

tion temperature of 200 ^{0}C. The magnetic properties have been characterized by Mössbauer spectroscopy (at about 300 K), vibrating sample magnetometer (VSM) and superconductive quantum interference device (SQUID) measurements from 2 K to 400 K.

In chapter 2 we present the basic principles of Mössbauer spectroscopy. The experimental techniques used in the current work are discussed in chapter 3. The results and discussions are presented in chapters 4 and 5. The concluding remarks are given in chapter 6.

Chapter 2

Basic principles of Mössbauer spectroscopy

Mössbauer effect is the recoil–free emission and absorption of γ photons with energy ranging from 10 keV to 100 keV [43]. It was discovered by Rudolf L. Mössbauer in 1957. The recoilless emission and absorption of γ–rays allow radiation with natural line width of about 14.6×10^{-9} eV [44] to be used in resonant absorption spectroscopy. This produces high resolution ($\triangle E/E = 3.5\times10^{-13}$) [43, 44], making Mössbauer spectroscopy a powerful tool in nuclear spectroscopy and condensed matter physics. It is capable of detecting weak interactions between the nucleus and its surrounding electrons [45, 47]. Mössbauer spectroscopy can provide information on magnetic, structural and bonding properties of materials. In this chapter we present the basic principles of Mössbauer spectroscopy. A brief discussion of hyperfine interactions is also given.

2.1 Mössbauer effect

When a nucleus in an excited energy state makes a transition to ground state, a γ–ray photon is emitted. The nucleus recoils during the γ–ray emission process. The energy of the emitted γ–ray photon is reduced by recoil and is thus less

than the energy difference between the excited and ground state energies. The γ–ray photon can therefore not be absorbed by another identical nucleus, i.e., resonant absorption is not possible.

This can be seen by considering an isolated nucleus of mass m and with excition energy E moving with velocity $\overrightarrow{V}$. If a γ–ray photon with energy E_γ is emitted in the direction of the emitting nucleus with velocity $\overrightarrow{v}$, the nucleus recoils with energy $\frac{1}{2}m(\overrightarrow{V}+\overrightarrow{v})^2$. Conservation of energy before and after the ejection of a γ–ray photon gives [45]

$$E+\frac{1}{2}mV^2 = E_\gamma+\frac{1}{2}m(\overrightarrow{V}+\overrightarrow{v})^2. \tag{2.1.1}$$

From equation (2.1.1) $E_\gamma = E-\frac{1}{2}mv^2-mvV = E-E_R-E_D$. The γ–ray photon energy is reduced by recoil ($E_R=\frac{1}{2}mv^2$) and thermal or Doppler ($E_D=mvV$) energies. The conservation of momentum gives [45]

$$mV = m(\overrightarrow{V}+\overrightarrow{v})+\frac{E_\gamma}{c}. \tag{2.1.2}$$

From equation (2.1.2) $v=-E_\gamma/mc$. The recoil energy can therefore be written as

$$E_R = \frac{E_\gamma^2}{2mc^2}. \tag{2.1.3}$$

E_R depends on the nuclear mass and energy of the γ–ray emitted. E_D has a distribution of values which are dependent on temperature. The average Doppler energy ($\overline{E}_D$) is related to the average translational energy ($\overline{E}_K$) according to the equation [45, 47]

$$\overline{E}_D = E_\gamma\sqrt{\frac{2\overline{E}_K}{mc^2}}. \tag{2.1.4}$$

The effects of recoil and thermal energy respectively result in the displacement and broadening of the statistical energy distributions of emitted and absorbed γ–ray photons as shown in Figure 2.1. The emission and absorption distributions of γ–ray photon energies are shifted from the excitation energy E by $-E_R$ and $+E_R$ respectively, and broadened by E_D into Gaussian distributions

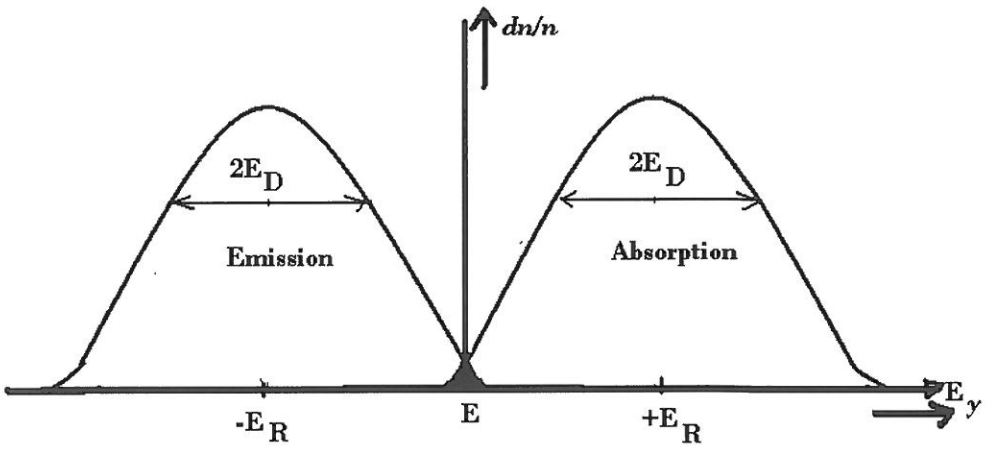

Figure 2.1: Resonant overlap in free atoms [45].

of width $2E_D$. There must be some overlapping (shown as shaded area) between the emission and absorption distributions for nuclear resonance to have a significant probability.

If the emitting nucleus is not free but fixed in a crystal lattice, recoil energy is taken up by the whole crystal. The nuclear mass m in equations (2.1.3) and (2.1.4) can be replaced by the mass of the whole crystal lattice. A typical crystal has about 10^{15} atoms. Therefore replacing nuclear mass m by the crystal mass M in equations (2.1.3) and (2.1.4), E_R and E_D become negligible. This is called Mössbauer effect, eliminating the effects of recoil and thermal broadening. If the recoil energy is not taken up by the whole crystal lattice, it will be transferred to the lattice by increasing its vibrational energy. In this case recoil energy is dissipated by creation of phonons. E_R is only transfered to lattice vibrations if it corresponds with the allowed increments otherwise it is transferred to the crystal as a whole ensuring recoilless emission or absorption of γ–ray photons.

2.2 Recoil–free fraction

The fraction of recoilless emission and absorption of γ–rays is related to the vibrational properties of the crystal lattice as [45]

$$f = exp\left(\frac{-E_\gamma^2 < x >^2}{(\hbar c)^2}\right). \tag{2.2.1}$$

$< x >^2$ is the mean-square vibrational amplitude of the emitting or absorbing nucleus. To increase the relative strength of the recoilless resonant process it is necessary to make the recoil–free factor as large as possible. The form of equation (2.2.1) indicates that f is large for low E_γ and small $< x >^2$ (strong lattice). This sets conditions for isotopes suitable for Mössbauer spectroscopy. ^{57}Fe, ^{119}Sn, ^{127}I, ^{125}Te and ^{195}Pt are examples of isotopes that can be used during Mössbauer experiments. ^{57}Fe is a typical Mössbauer nucleus produced by the radioactive decay of ^{57}Co. It is used to study compounds that contain Fe.

According to the Debye model [45] recoil free fraction varies with temperature according to the equation

$$f = exp\left[-\frac{6E_R}{k_B\theta_D}\left[\frac{1}{4} + \left(\frac{T}{\theta_D}\right)^2 \int_0^{\theta_D/T} \frac{xdx}{e^x - 1}\right]\right], \tag{2.2.2}$$

where $x = \hbar k_B T$ and θ_D is the Debye temperature defined as

$$\theta_D = \frac{\hbar\omega_D}{k_B}. \tag{2.2.3}$$

From equation (2.2.2) f is maximum when θ_D is large and the measuring temperature (T) is low. At $T = 0$ equation (2.2.2) gives

$$f = exp\left(\frac{-3E_R}{2k_B\theta_D}\right). \tag{2.2.4}$$

2.3 Hyperfine interactions

The electrostatic and magnetic interactions of a nucleus with its own environment are known as "hyperfine interactions". These interactions can be measured during Mössbauer experiments and are discussed in the following sections.

2.3.1 Isomer shift

The nuclear size changes when a nucleus makes a transition from excited to ground state or vice versa. The change in nuclear size results in the changes in Coulombic forces between the nuclear charge and the extra nuclear electrons. This results in a shift but not splitting of nuclear energy levels known as isomer or chemical shift. This effect is shown in Figure 2.2 (a). The expression for isomer shift is give by [47]

$$\delta = \left(\frac{Ze^2}{10\epsilon_0}\right)\left[|\psi_A(0)|^2 - |\psi_S(0)|^2\right]\left(R_{ex}^2 - R_{gd}^2\right). \tag{2.3.1}$$

Z is the atomic number, e is the electronic charge and ϵ_0 is the permittivity in free space. $|\psi_A(0)|^2$ and $|\psi_S(0)|^2$ are s–electron densities at the nuclear sites of the absorber and source nucleus. R_{ex} and R_{gd} are nuclear radii in the excited and ground states. This energy shift is usually quoted in mm/s rather than in energy units. "1 mm/s"is proportional to 4.8×10^{-8} keV for ^{57}Fe isotope. The change in nuclear radius is constant for a Mössbauer transition. Equation (2.3.1) can therefore be written as

$$\delta = K\left(|\psi_A(0)|^2 - |\psi_S(0)|^2\right) \tag{2.3.2}$$

where K is a constant depending on the change in nuclear radii. During a Mössbauer experiment energy shifts are measured relative to the centroid of a metallic iron foil spectrum recorded at room temperature. The measurements of isomer shift are therefore independent of the nature of the source [45]. Equation (2.3.2) can therefore be reduced to

$$\delta = K_0 - K|\psi_A(0)|^2 \tag{2.3.3}$$

where K_0 is a constant. The isomer shift is therefore only dependant on the s–electron density of the absorber. It can therefore give information on the changes of the orbital occupation in the valence shell of the absorber atom and can be used to investigate oxidation states and covalency effects [45].

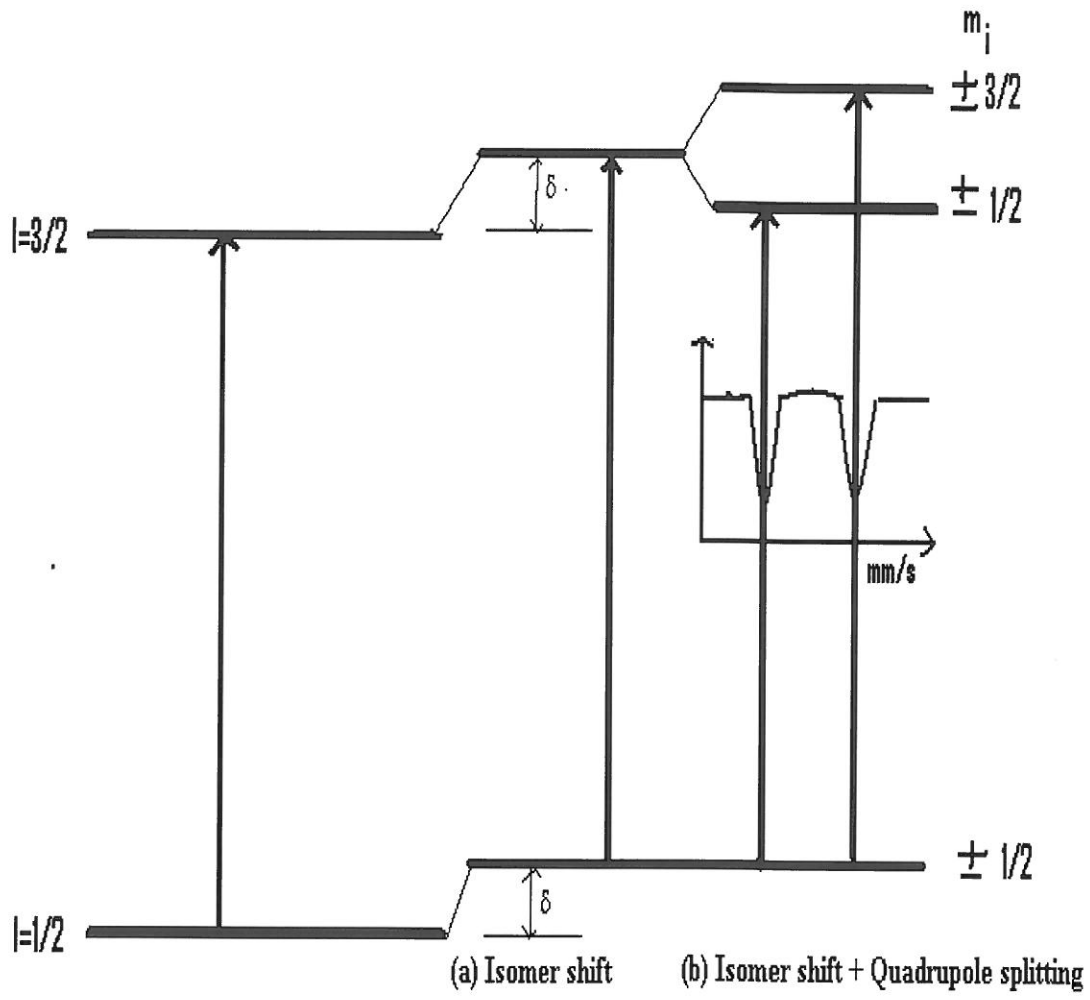

Figure 2.2: (a) Isomer shift, (b) Isomer shift and quadrupole splitting [43].

2.3.2 Electric quadrupole splitting

The electric quadrupole splitting results from the interaction between the nuclear quadrupole moment ($\overrightarrow{Q}$) and the electric field gradient ($\nabla\overrightarrow{E}$) at the crystal lattice. The electric quadrupole interaction is described by the Hamiltonian

$$H = -\frac{e}{6}\overrightarrow{Q}.\nabla\overrightarrow{E}. \tag{2.3.4}$$

It results in the splitting of a nuclear energy level with angular momentum I into $2I+1$ sublevels. The energies of the sublevels are given by [45]

$$E_Q = \frac{eV_{zz}Q}{4I(2I-1)}\frac{3m_I^2 - I(I+1)}{4I(2I-1)}\left(1+\frac{\eta^2}{3}\right)^{1/2}. \tag{2.3.5}$$

$V_{zz} = \partial^2V/\partial z^2$ is the component of the electric field gradient tensor along the z axis and $\eta = [\partial^2V/\partial x^2 - \partial^2V/\partial y^2]/q$ is an asymmetry parameter. m_I is the magnetic quantum number of the nuclear state considered and takes values from I to $-I$. The ^{57}Fe Mössbauer transition taking place between $I = 3/2$ and $I = 1/2$ spin states. The I =3/2 energy state splits into two energy levels corresponding to $m_I = \pm 3/2$ and $m_I = \pm 1/2$ and the I =1/2 energy state does not split. The transitions between the sublevels take place provided the selection rules ($\triangle I = 0, \pm 1$) are satisfied. The two possible transitions shown in Figure 2.2 can be seen as two absorption peaks during a Mössbauer experiment. The peaks are separated by energy [45]

$$\nabla = \frac{1}{2}eV_{zz}Q, \tag{2.3.6}$$

called the quadrupole splitting.

2.3.3 Magnetic splitting

A nucleus with a magnetic moment ($\overrightarrow{\mu}$) and spin quantum number (I) will have a dipole interaction with the magnetic field ($\overrightarrow{B}$). This interaction is described by the Hemiltonian

$$\overrightarrow{H} = -\overrightarrow{\mu}.\overrightarrow{B} = -g\mu_N\overrightarrow{I}.B \tag{2.3.7}$$

The energies of the nuclear levels are given by [45]

$$E_m = -\frac{\mu B}{I} m_I = -g\mu_N B m_I. \tag{2.3.8}$$

m_I is the magnetic quantum number, μ_N is the nuclear magneton, g is the Lande's factor = 2 and B is the magnetic field. B depends on the combination of both the internal and applied magnetic field. In this work the Mössbauer measurements were taken under zero applied fields. The magnetic splitting is due to only the internal magnetic fields. In the case of ^{57}Fe nucleus I=3/2 splits into m_I = +3/2, +1/2, -1/2 and -3/2 sublevels. The I = 1/2 ground state splits into m_I = +1/2 and -1/2 sublevels. The allowed transitions according to the selection rules ($\triangle$I = 0, $\pm$1) are shown in Figure 2.3. The six absorption lines are seen as a six line Mössbauer spectrum during a Mössbauer experiment.

When the nuleus experiences both quadrupole and magnetic interactions, the energy eigen values are given by [44]

$$E_{QM} = \frac{e^2qQ}{4}\left((-1)^{|m_z|+1/2}\right)\left(\frac{3cos^2\theta - 1}{2}\right) - g\mu_N \overrightarrow{I}.\overrightarrow{B}. \tag{2.3.9}$$

The effect of combined magnetic and quadrupole interactions is the shifting of the nuclear energy levels by [44]

$$\epsilon = \frac{e^2qQ}{4}\left(\frac{3cos^2\theta - 1}{2}\right). \tag{2.3.10}$$

θ is the angle between the magnetic field axis and the major axis of the electric field gradient tensor.

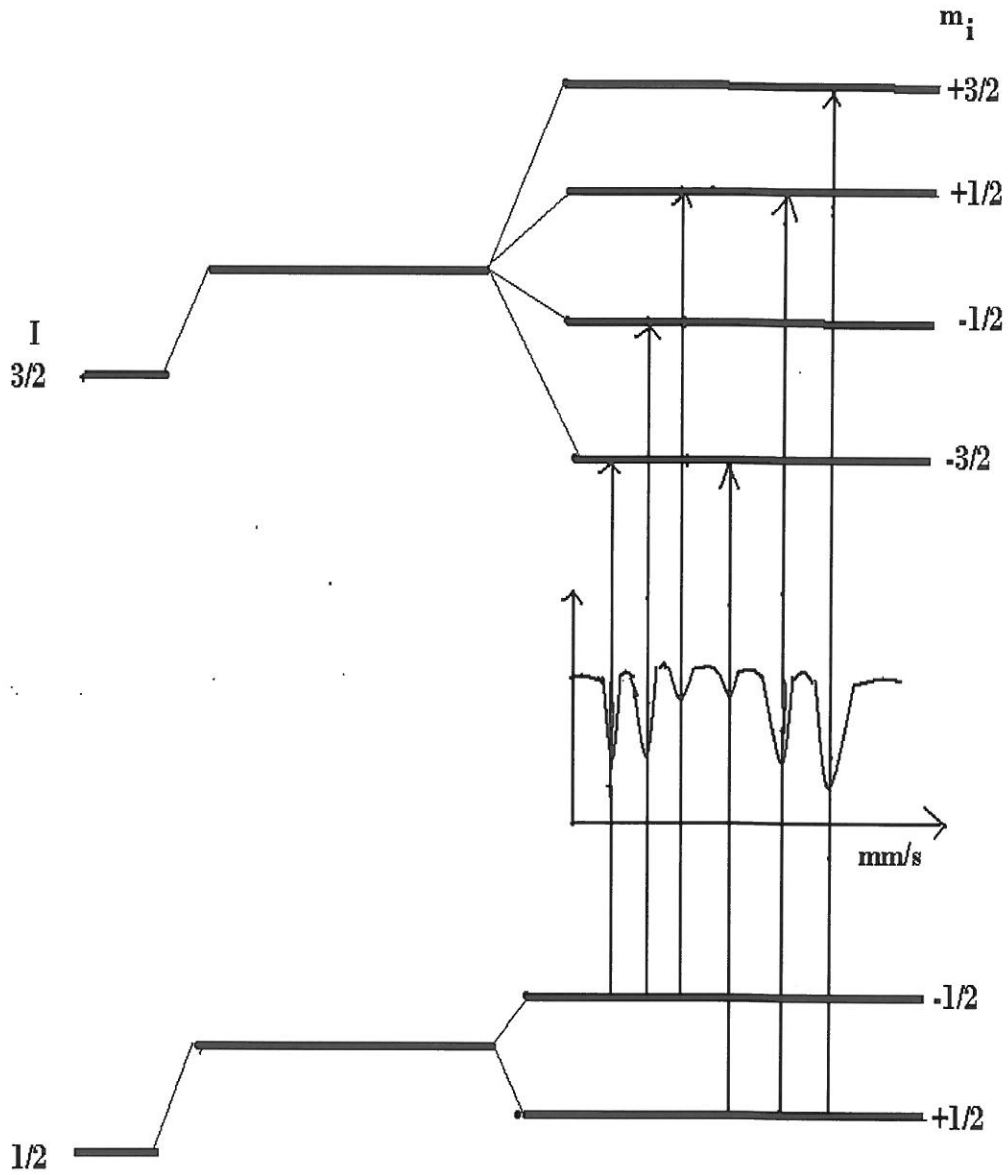

Figure 2.3: Magnetic splitting in ^{57}Fe nucleus [43].

Chapter 3

Experimental details

Ferrites are generally prepared by solid state reaction or high energy ball milling as discussed in section 1.2. This requires double high temperature heat treatment stages. Ferrite nanoparticles can be prepared by using high energy ball milling and wet chemical methods. The synthesis of fine powders has been the subject of recent intensive research. Several reports have appeared in the literature which use wet chemical methods such as co–precipitation [20, 21], hydrothermal [18, 19], sol–gel [23], forced hydrolysis [25] and combustion [23] methods. In this work we have produced bulk and nanosized $CdFe_2O_4$ and $Zn_xMn_{1-x}Fe_2O_4$ ferrites using solid state reaction, high energy ball milling and glycolthermal reaction. The procedures followed during sample preparation are discussed in this chapter. The compounds produced were characterized by Mössbauer spectroscopy, magnetizations and XRD measurements. A brief discussion of these sample measurements techniques is also given.

3.1 Sample preparation

3.1.1 Solid state reaction

The $CdFe_2O_4$ oxide was produced by solid state reaction. The starting materials were CdO (99 %) and Fe_2O_3 (99.995 %). The stoichiometric proportions

of the oxides were weighed using an electronic balance (Precisa 205A SCS) and mixed. During the mixing process the oxide mixture was hand ground for about 30 minutes using agate mortar and pestle in liquid medium (ethanol). The grinding was done under a 100 W study lamp. This is helpful in the drying process of the mixture. The dried powders were pressed in a stainless steel evacuated die under a pressure of about 2 tons/cm^2 to form pellets. The pressure was applied for two minutes. The pellets were initially sintered at 950 ^{0}C. The products were reground to fine powders which were again pressed into pellets and finally sintered at 1050 ^{0}C. All the heat treatments were done in air for 12 hours. After each heat treatment samples were allowed to slowly cool to room temperature.

3.1.2 High energy ball milling

A Retch high energy planetary ball mill (type PM 400) was used to grind $CdFe_2O_4$ ferrite sample produced by solid state reaction into a fine powders. The oxide was loaded into hardened steel vials with hardened steel balls. The ball–to–mass ratio was 20:1. The planetary ball mill was operated at 200 rev/min. The sample was milled for 50 hours. After selected milling times (1 h, 3 h, 5 h, 10 h, 20 h, 30 h, 40h and 50 h) some powders were removed for analysis. The aim was to systematically study the effect of high energy ball milling on the properties and to produce $CdFe_2O_4$ nanoparticles.

3.1.3 Glycolthermal reaction

We have used a wet chemical method called glycolthermal reaction [42] to produce $Zn_{0.5}(Co, Ni)_{0.5}Fe_2O_4$, $Zn_xMn_{1-x}Fe_2O_4$ and $Cu_xMn_{1-x}Fe_2O_4$ ($0 \leq x \leq 1$) ferrites. The starting materials were chlorides or nitrates. The required stoichiometric amounts of chlorides or nitrates were mixed. 5 M solution of sodium hydroxide (NaOH) was used as a precipitant. It was slowly added to the nitrate mixture under rapid stirring until the pH was about 10. The precipitate

was washed several times with deionized water to remove chlorides or nitrates. During the washing process the precipitate was filtered using ashless Glass microfibre (GF/F Whatman) filter papers. The clean precipitate could be confirmed by the addition of a standard silver nitrate solution or phenolphthalein. The product was dispersed in 300 ml of ethylene glycol and placed in a 600 ml stainless steel pressure vessel (Watlow series model PARR 4843 reactor). The temperature was allowed to increase to 200 ^{0}C. The pressure rose to about 110 psi. These conditions were kept for 6 hours while stirring at 200 rev/min. The cooled products were filtered and re–washed in deionized water and finally with ethanol. The recovered synthesized powders were dried under a 250 W infrared lamp and homogenized using agate mortar and pestle.

3.2 Mössbauer measurements

In a Mössbauer experiment a suitable radioactive source is used to irradiate the specimen under investigation. ^{57}Co is used to study samples with iron. Figure 3.1 shows the decay scheme of ^{57}Co from the 837 keV ($I = 7/2$) energy state to ^{57}Fe with lower energy state of 136 keV by electron capture. These photons are emitted during transitions from the $I = 3/2$ to $I = 1/2$ ground states. The 14.41 keV energy peak is used in the Mössbauer experiment.

In order to use the source as a spectroscopic tool, the energy of the source is varied. This is achieved by Doppler shifting the energy of the photons. Moving a source at velocity of 1 mm/s towards the sample increases the energy of photons by 14.4 keV $(v/c) = 4.8 \times 10^{-8}\ eV$. The mm/s is a unit used in Mössbauer experiments. This is equivalent to $4.8 \times 10^{-8}\ eV$ for ^{57}Fe.

A Mössbauer spectrometer consists of a source which may be moved relative to the sample and a counter to monitor the intensity of the beam after it has passed through the sample. The basic experimental set–up in transmission geometry consists of a Mössbauer source and a detector placed behind the specimen being measured. The γ–ray photons transmitted through the sample

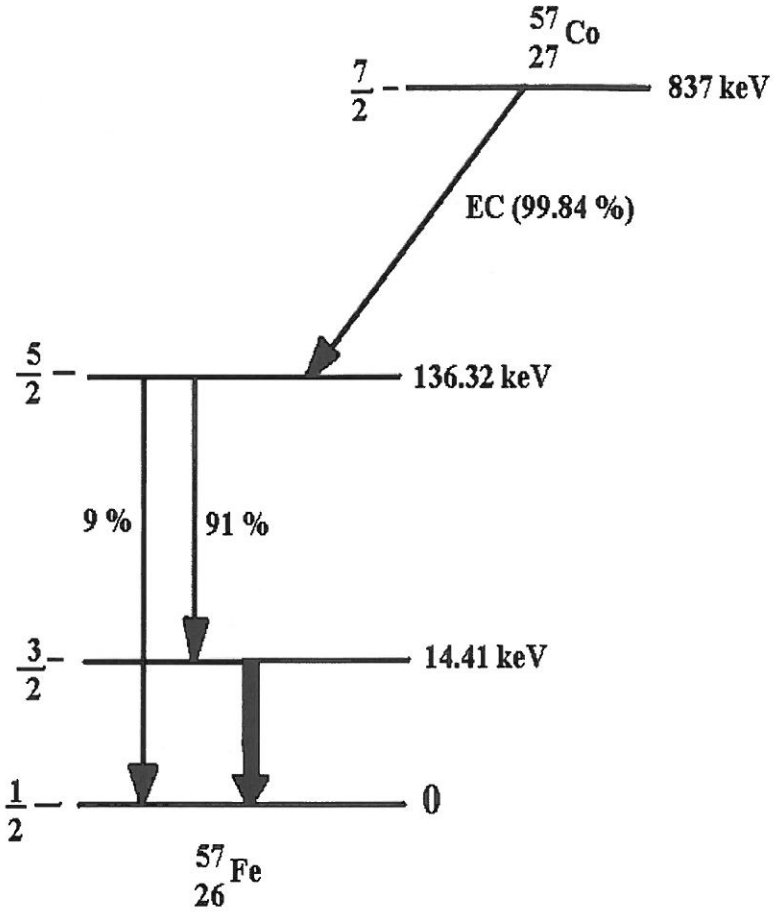

Figure 3.1: Nuclear Decay scheme of ^{57}Co [45].

are detected by a detector and the corresponding amplified pulses are registered in different channels according to their energies. The Mössbauer spectrum develops with time as counts are accumulated in different channels. The spectrum thus consists of "dips" and "high" intensity counts. The "dips" and "high" intensity counts are at the energies where resonant absorption and maximum transmission occur respectively. The Mössbauer spectrum is a plot of the transmitted intensity against the source velocity (beam energy).

In a constant velocity Mössbauer spectrometer, the transmitted γ–ray photons are recorded at a constant velocity in a fixed period of time. The spectrum is accumulated as the constant velocity is changed. In this method the spectrum is accumulated step wise with one velocity at a time. In the current work we have used a more common approach where the whole velocity range is rapidly scanned. By numerous repetition of the velocity sweeps, states for individual velocities (energies) are accumulated simultaneously. The Mössbauer measurements were performed at room temperature (300 K). The spectrometer was connected as shown in Figure 3.2. The frequency (2.5 Hz) of the source was selected from the function generator. A triangular wave output was selected so that the source moves at constant acceleration. The MCS32 card (used for data acquisition) was connected to both linear amplifier output and Mössbauer drive unit as shown in Figure 3.2. The Recoil software package was used for the analysis of the Mössbauer data.

3.3 Magnetization measurements

Magnetization arises in materials due to the presence of magnetic moments of constituents atoms. The magnetic moments originate from the electronic motions and intrinsic spin of electrons as discussed in reference [28, 46]. The total magnetic moments of a sample per unit volume is called magnetization (M). M is usually determined under the influence of a magnetic field. The field can be considered as a stimulus which affects the alignments of the magnetic

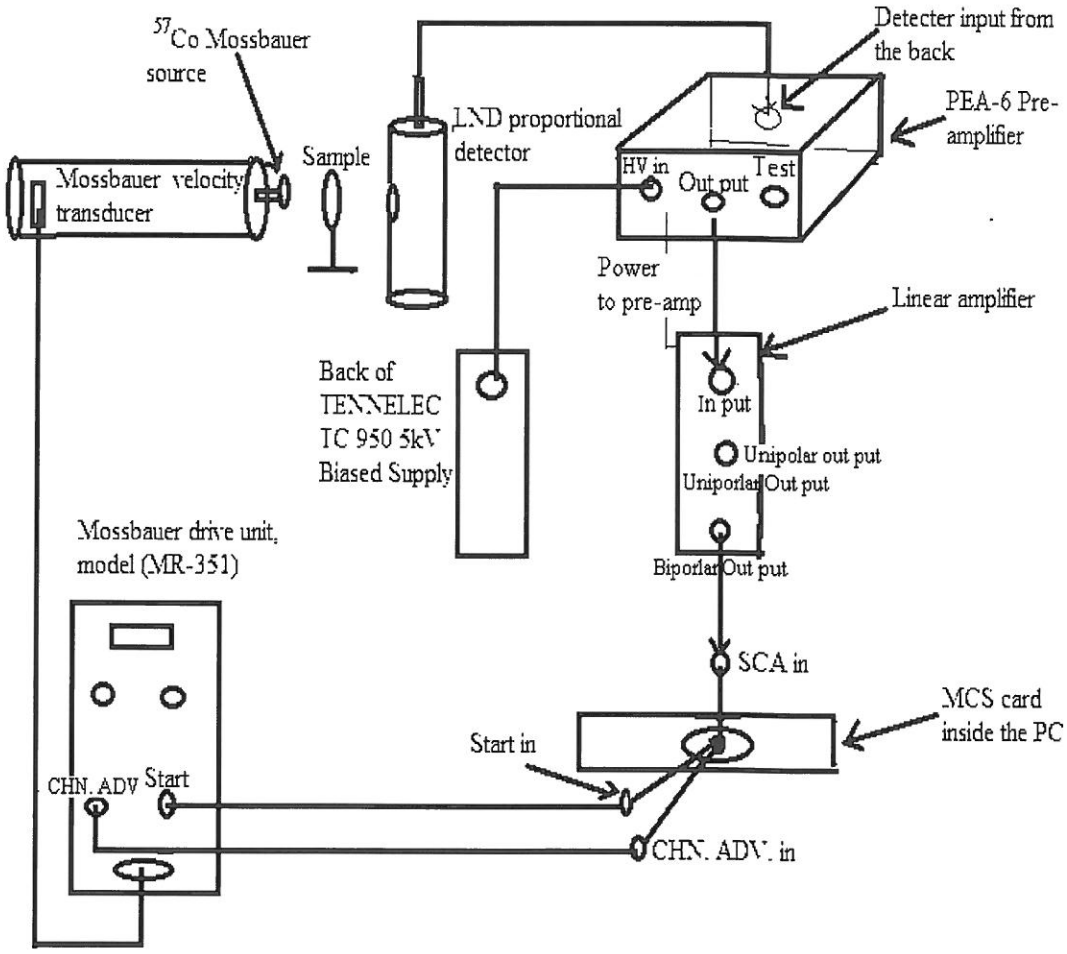

Figure 3.2: Experimental set–up for the Mössbauer spectrometer.

moments in the field direction. In practice we want to know how M varies with temperature and applied magnetic field. The definition of magnetization as magnetic moments per unit volume turns out to be unsuitable because the volume is dependent on the temperature (thermal expansion) or magnetic field (magnetostriction). Magnetization (σ) can be defined per unit mass as

$$\sigma = \frac{M}{\rho}. \tag{3.3.1}$$

where M is the magnetic moment and ρ is the density. The response function of magnetization of the sample under the influence of a magnetic field is called susceptibility and is defined as

$$\chi = \frac{\mu_0 M}{B}, \tag{3.3.2}$$

where $\mu_0 = 4\pi \times 10^{-7}$ v_s/Am. Measurements of magnetization using magnetometry are discussed in [28]. In this work we have studied magnetization as a function of magnetic field or temperature using a Lakeshore vibrating sample magnetometer (VSM) at UKZN and Quantum Design Superconductive Quantum Interference Device (SQUID) of quantum design make in the Deparment of Physics at the University of Johannesburg (UJ).

3.4 X–ray diffraction

X–rays were discovered in 1895 by Wilhelm Roentgen while experimenting with cathode rays (electrons) in an evacuated glass tube containing two electrodes between which a high voltage was applied. Roentgen noticed that some of radiation from such a tube could easily penetrate through materials such as card board, wood and sheets of metals. He referred to these rays as X–rays. The X–rays originate from the sudden stopping of fast moving electrons at the walls of the tube or at the metal plate which served as an anode. X–rays are now commonly produced by the bombardment of a metal target (anode) by electrons accelerated from the cathode by high voltage as shown in Figure 3.3.

At high accelerating voltages, the impinging electrons have enough energy to eject electrons from core–levels of the target atoms. X–rays are also emitted when electrons in higher energy states move down to fill the lower energy states. If 1s (k–shell) electrons are ejected by the impinging electrons beam, L–shell ($2p_{3/2}$, $2p_{1/2}$) or M–shell ($3p_{3/2}$, $3p_{1/2}$) electrons fill the k–shell. On dropping down, kα_1 and kα_2 or kβ_1 and kβ_2 x–rays are emitted. Monochromatic X–ray beams are achieved by using a filters or a monochromators. Monochromatic X–ray beam of wavelength λ is diffracted by a crystal when the condition for Bragg d reflection [48–50]

$$n\lambda = 2dsin\theta \tag{3.4.1}$$

is satisfied. n is an integer and d is the distance between the adjacent atomic planes in a crystal. The Bragg angle θ is the glancing angle at which the x–rays beam strikes the specimen.

In the powder X–ray diffraction (XRD) method, a powdered sample can rotated in the X–ray beam. Each particle in the sample acts as a crystal mounted at random with respect to the beam. As the sample is rotated, different planes at different Bragg angles diffract. Diffraction takes place for the planes of particle oriented such that the Bragg equation (3.4.1) holds. The spectrum therefore consists of different diffraction lines at different 2θ values. From equation (3.4.1) if an x–ray beam of a known wavelength λ is used, the spacing of the planes of atoms (d) can be calculated. In the case of ferrite materials studied in the current work, the crystal structure is cubic. Hence d is related to the lattice parameter (a) by [48]

$$a = d\sqrt{h^2 + k^2 + l^2}. \tag{3.4.2}$$

We only need to assign the correct Miller indices (h, k, l) to each diffraction peak. In the present work, XRD was used to characterize the samples. The XRD measurements were carried out in the Department of Physics at the University of Free State and in the Department of Geology at the University of KwaZulu–Natal.

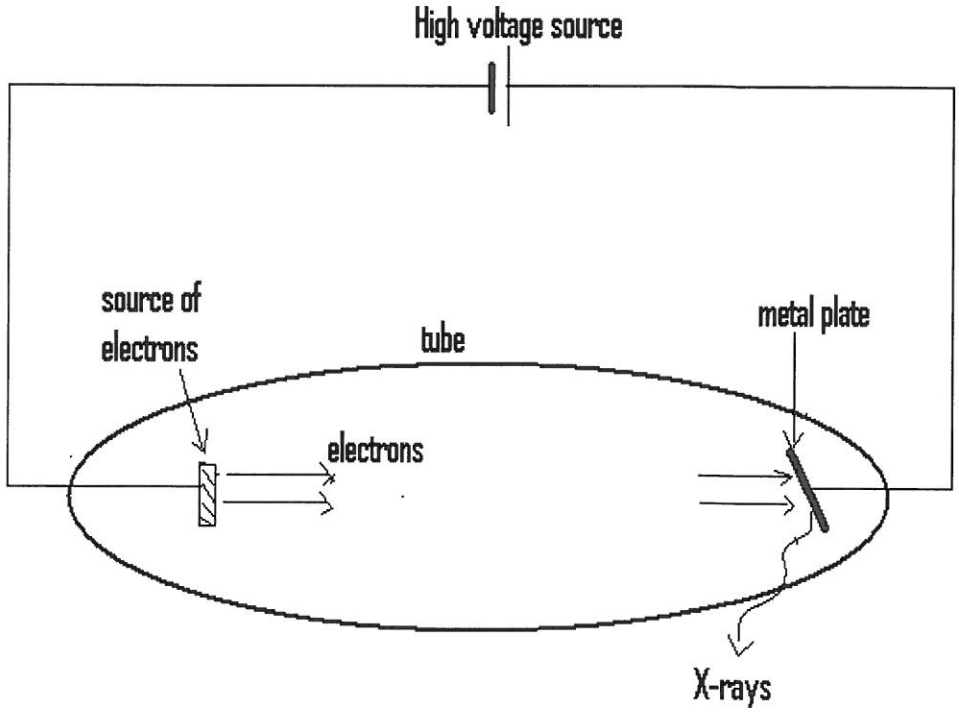

Figure 3.3: Generation of x–rays [47].

A monochromatic beam of Co k_α radiation of wavelength $\lambda = 1.78897$ Å, was used in the measurements. The nature, size of the unit cell and quality of the samples were determined from XRD.

Chapter 4

Magnetic properties of bulk and nanosized $CdFe_2O_4$ oxides

The particle sizes have significant effects on the properties of materials. The Curie temperature (T_C) of the bulk normal spinel $ZnFe_2O_4$ is about 10 K [5, 14]. An increased magnetic transition temperature in milled $ZnFe_2O_4$ fine powders to about 40 K was observed. This enhancement of T_C was associated with the increase in the population of Fe^{3+} ions at A sites. Cd is a larger size atom compared to Zn. In this work we have produced $CdFe_2O_4$ by solid state reaction and systematically reduced particle sizes to nanometer scale. The chemical and structural disorders induced by high energy ball milling are investigated. In this chapter we present the variation of the magnetic properties of $CdFe_2O_4$ as a function of milling time.

4.1 X-ray diffraction results

The structural analysis of the as prepared and milled $CdFe_2O_4$ ferrite samples were performed by X–ray diffraction (XRD) technique using Co K_α radiation. Figure 4.1 shows the variation of the XRD patterns for different of milling times (from 0 h to 50 h). The most significant peaks were successfully indexed to cubic spinel structure. A small impurity peak at $2\theta = 53^0$ is observed in

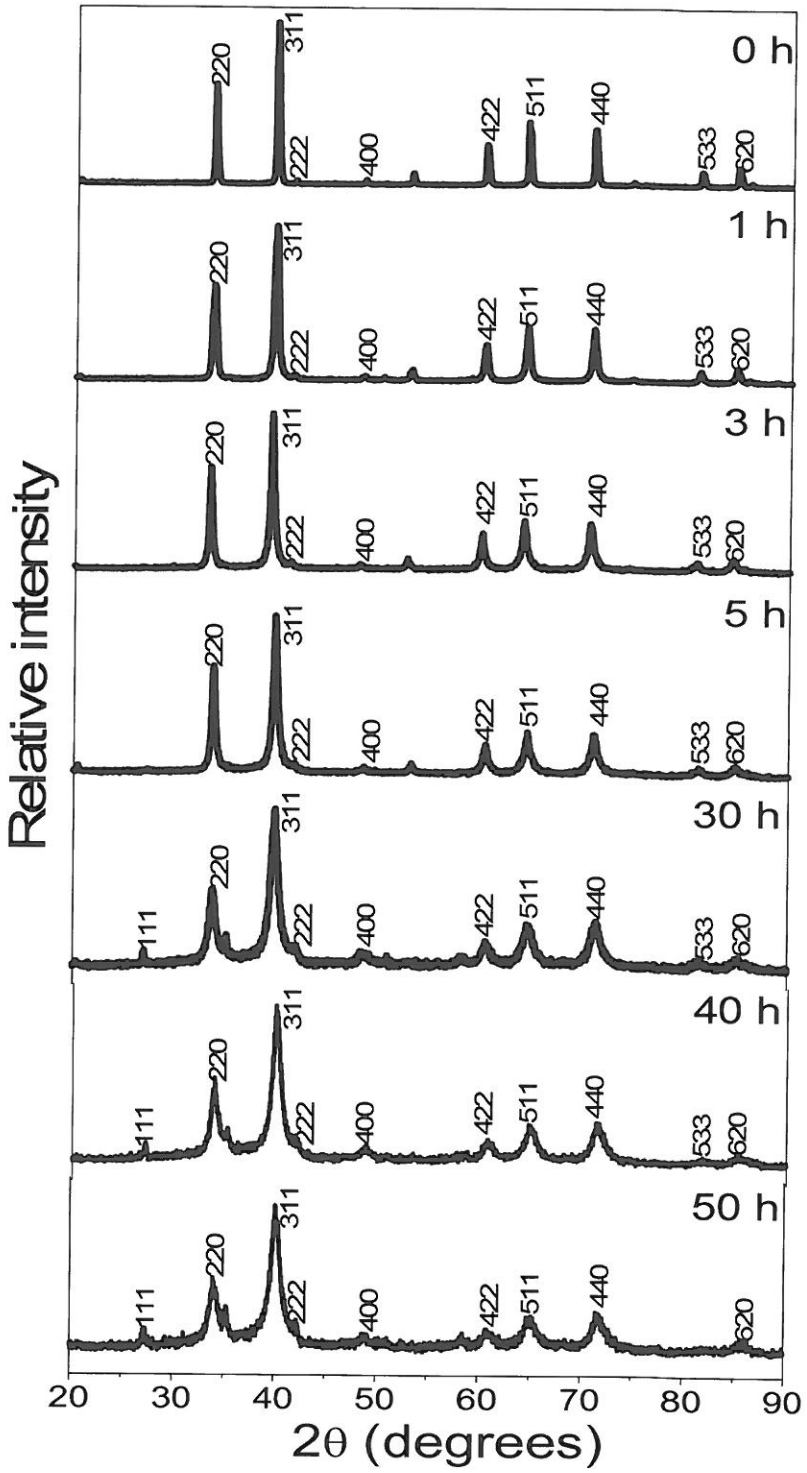

Figure 4.1: Variation of XRD patterns for $CdFe_2O_4$ with milling time.

the as prepared (0 h), 3 h and 5 h milled samples. This may be due to an intermediate α–Fe_2O_3 phase. This impurity peak disappears after milling for more than 20 hours. The broadening of the XRD peaks with increasing milling time indicates reducing particle size. The particle sizes were estimated from the most intense 311 XRD peaks using the Debye-Scherrer formula [51, 52]

$$D = \frac{0.9\lambda}{\beta \cos\theta}. \tag{4.1.1}$$

D is the particle size, λ is X–ray wavelength, β is the full width at half maximum of the 311 XRD peak and θ is the Bragg angle. The values of grain size as a function of milling time are shown in Table 4.1 and plotted in Figure 4.2. After milling for 50 hours the grain sizes were reduced from about 39 nm to 9 nm. Milling has a significant effect on particle diameters. As shown in Figure 4.2, a fast initial decrease of grain size upon milling occurs. After 10 hours of milling, a slower reduction of grain size with further milling is observed. This is limited by the size of the steel balls used in the milling process for dry grinding. The values of lattice parameters deduced from the XRD data are also shown in Table 4.1. A general decrease in the size of the lattice constant with increasing milling time may be due to structural disorder induced by milling. The x–ray densities can be calculated from the values of lattice parameters (a) by using the formula [53]

$$\rho_X = \frac{8M}{N_A a^3}. \tag{4.1.2}$$

8 is the number of atoms in the unit cell of a spinel lattice, M is the molecular weight of the sample and N_A is the Avogadro's number. The values of ρ_X are shown in Table 4.1 as a function of milling time. The average X–ray density calculated for our samples is 5.77 g/cm^3. This is comparable to values found for similar compounds [52, 54]. The ρ_X reflects on the packing of the atoms in a unit cell. This is expected to be higher than the bulk densities.

Table 4.1: Variation of grain size (D), lattice parameter (a) and x–ray density (ρ_X) with milling time.

MT (h)	D (nm)	a (Å)	ρ_X (g/m^3)
	$\pm$ 0.02	$\pm$ 0.01	$\pm$ 0.01
0	39.43	8.75	5.71
1	22.54	8.76	5.70
3	23.54	8.81	5.60
5	18.87	8.72	5.76
10	11.43	8.73	5.75
20	10.13	8.70	5.81
30	11.11	8.71	5.78
40	10.55	8.67	5.86
50	9.07	8.63	5.95

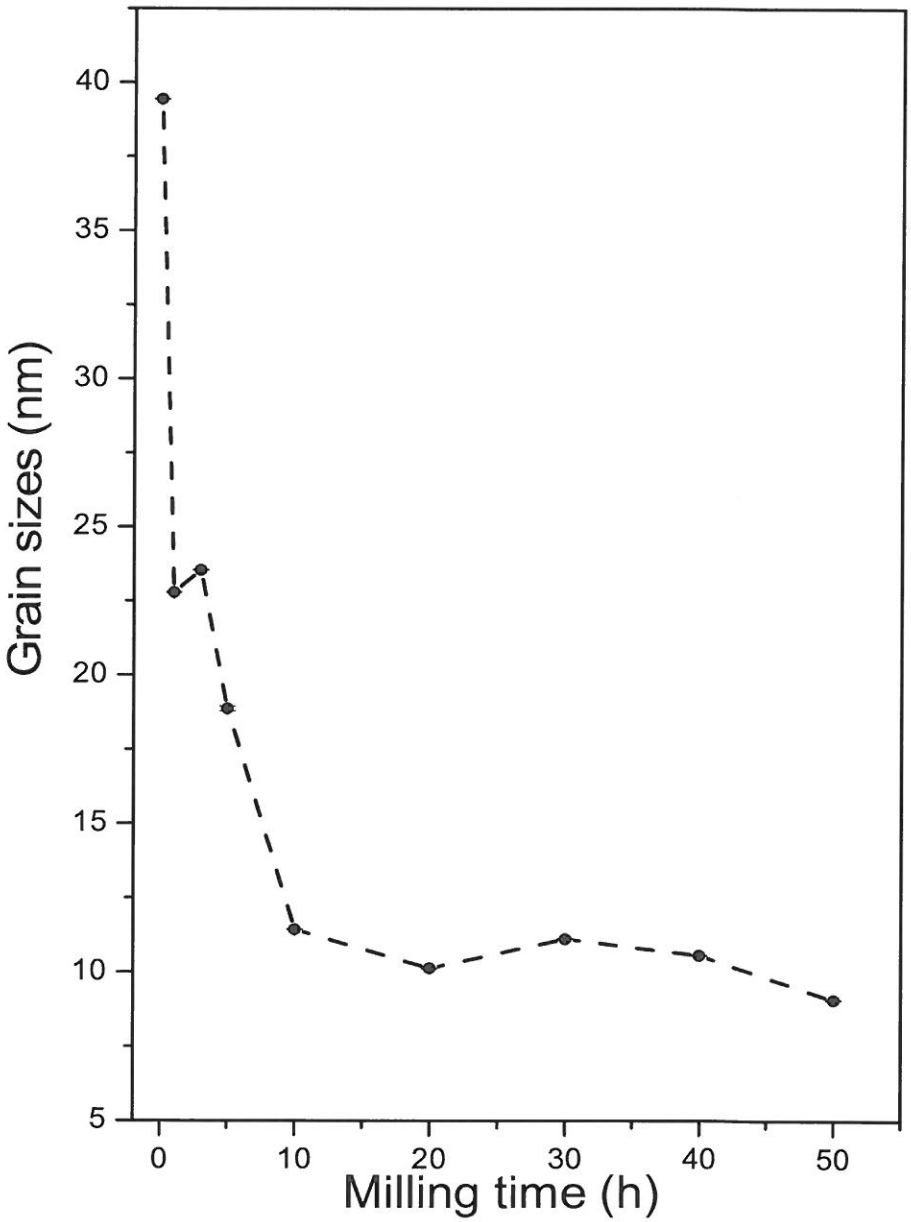

Figure 4.2: Variation of grain size for $CdFe_2O_4$ with milling time.

4.2 Mössbauer spectroscopy results

The variation of Mössbauer spectra with milling time is shown in Figure 4.3. The spectra could be resolved into two quadrupole doublets. The doublets indicate paramagnetic nature in the $CdFe_2O_4$ oxide at room temperature. The points are the experimental and the lines are fitted data. The doublets can be associated with Fe^{3+} ions in paramagnetic spin state at A or B site. The values of isomer shifts, quadrupole splitting, line widths and Fe fractions at A and B sites deduced from the fitted spectra are listed in Table 4.2. The doublets were allocated to A or B site based on the fitted data of isomer shifts, quadrupole splitting and line width. The A site isomer shifts and quadrupole splitting are generally lower than B sites values because the A site isomer shift is higher than the B sites values [6].

The isomer shifts give information on s–electron charge distribution of the Fe ions. There is no significant change in isomer shifts upon milling. This is expected since the Fe concentration is not changing with milling. The line widths and quadrupole splitting also do not change significantly with crystal size reduction.

The areas of fitted doublets represent Fe fractions on A or B sites. The doublet areas indicate the fractions of Fe ions at A or B sites. The Fe fractions at A or B sites are also shown in Table 4.2. The unmilled (0 h) and 1 h milled oxides indicate lower content of Fe atoms at A sites. This implies A sites are occupied by Cd ions. The distribution of Fe ions between A and B sites in the 3 h milled sample is similar. This behaviour is similar to a normal spinel. A decrease in A site Fe concentration with further milling is observed. Milling appears to force some of the Fe ions from A to B sites. This is associated with chemical disorder induced by milling.

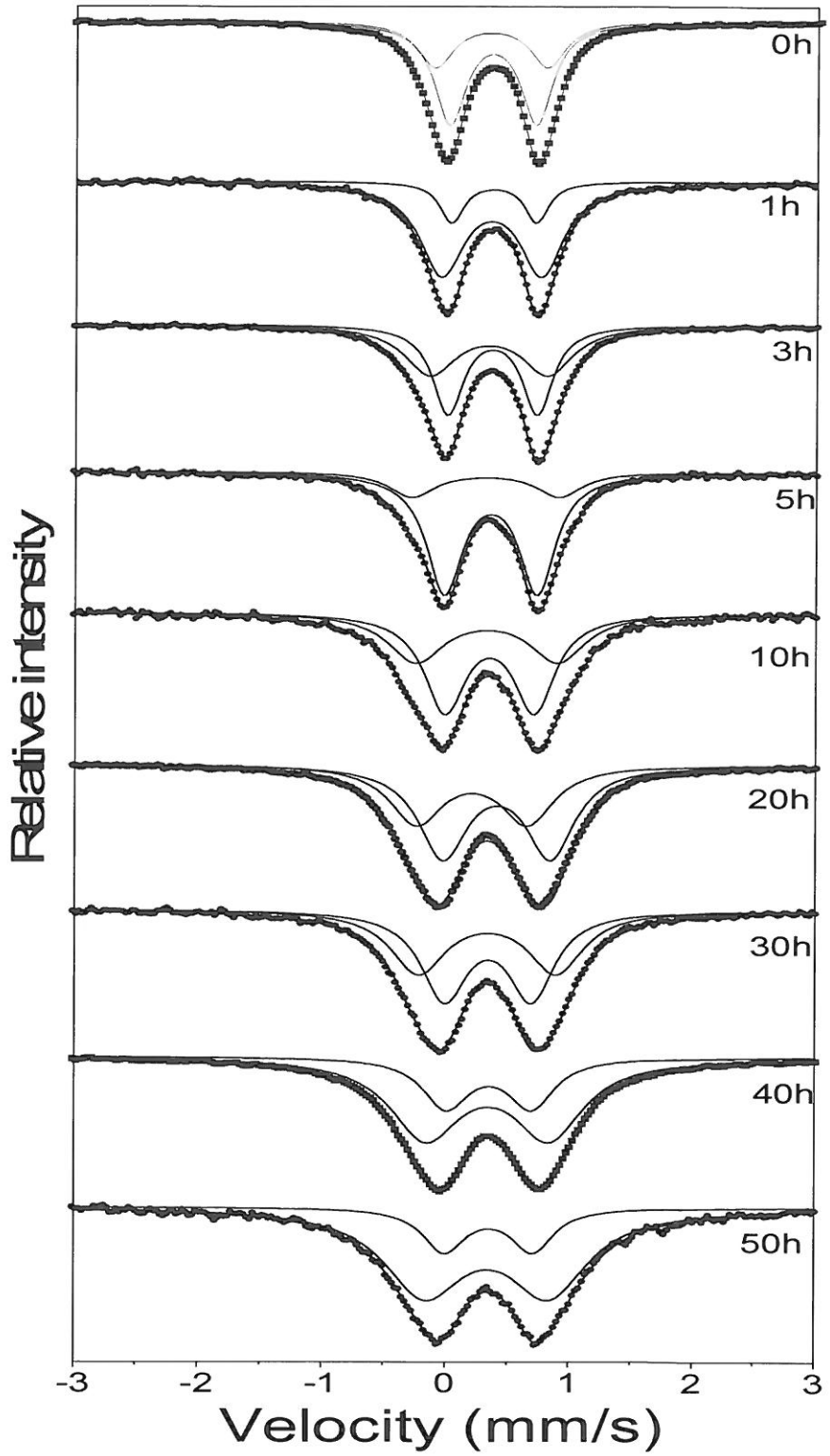

Figure 4.3: Variation of Mössbauer spectra for $CdFe_2O_4$ as a function of milling time.

Table 4.2: Variation of isomer shift (δ), quadrupole splitting (ε), line width (l) and Fe^{3+} fraction (f) on A and B sites for $CdFe_2O_4$ oxide with milling time.

	δ (mm/s)		ε (mm/s)		l(mm/s)		f(%)	
MT (h)	δ_A	δ_B	ε_A	ε_B	l_A	l_B	f_A	f_B
	± 0.006	± 0.008	±0.03	± 0.04	±0.01	± 0.02	±0.5	±0.6
0	0.360	0.366	0.70	0.91	0.16	0.18	33.9	66.1
1	0.386	0.368	0.69	0.81	0.12	0.22	19.6	80.4
3	0.378	0.348	0.72	0.95	0.15	0.25	51.7	48.3
5	0.367	0.330	0.75	1.19	0.18	0.23	78.6	21.4
10	0.359	0.330	0.72	1.15	0.20	0.28	59.2	40.8
20	0.418	0.210	0.87	0.89	0.24	0.26	58.6	41.1
30	0.348	0.343	0.70	1.12	0.23	0.27	53.6	46.4
40	0.356	0.346	0.69	1.00	0.23	0.35	70.5	29.5
50	0.353	0.341	0.71	1.01	0.21	0.39	21.7	78.3

4.3 Magnetization results

The magnetizations of the $CdFe_2O_4$ ferrite samples were measured using a vibrating sample magnetometer (VSM) from 10 K to 400 K. Figure 4.4 (a) shows typical variation of hysteresis loops with milling time. The "S"shaped magnetization curves with very small coercive fields indicate superparamagnetic nature of the fine particles. There is no significant change in coercivity with reduction in particle size. This is unlike the behaviour observed in $NiFe_2O_4$ and $Cu_{0.5}Ni_{0.5}Fe_2O_4$ compounds where the coercive fields increase with reducing grain size [6, 31]. This was explained on the basis of domain transformation from single– to multi-domain behaviour with reduction in particle size.

A general increase in saturation magnetization with reducing particle size is observed. This can be explained by the redistribution of Cd and Fe^{3+} atoms at both A and B sites as the grain size reduces. Bulk $CdFe_2O_4$ is a normal spinel with Fe ions equally distributed between A and B sites. Since A and B sublattices are aligned antiparallel, $CdFe_2O_4$ is expected to have very small magnetization. Increasing magnetization with increasing milling time (reducing particle size) relates well the Mössbauer results indicating reduction of Fe^{3+} content at A sites with milling.

The variation of hysteresis curves as a function of sample measuring temperature is shown in Figures 4.4 (b) and (c) for the as prepared (0 h) and 50 h milled samples, respectively. A larger increase in magnetization with reduction in temperature occurs in the 50 h milled sample. The coercive fields also depend on the on the temperature. The magnetic parameters deduced from the magnetization curves are shown in Table 4.3. A plot of coercive fields as a function of sample measuring temperature is shown in Figure 4.5. A fast decrease in coercivity with increasing temperature is observed up to about 100 K. The coercive fields then slowly reduces with further increase in temperature. The coercive fields of the as prepared sample increases from about 38 Oe at room temperature to 197 Oe at 10 K. A larger increase from about 9 Oe to

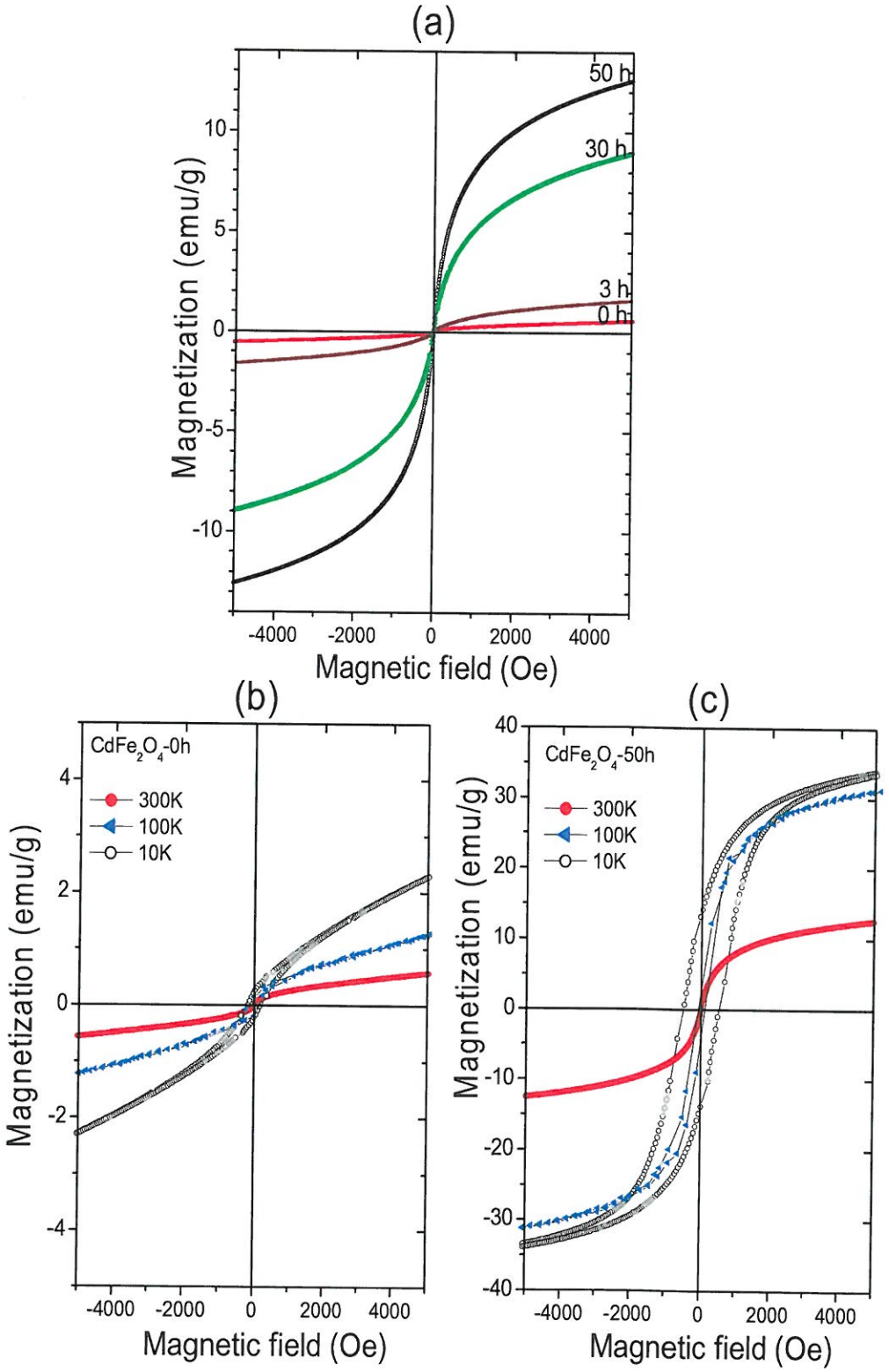

Figure 4.4: Variation of magnetization curves for $CdFe_2O_4$ oxides with milling time at 300 K, as prepared and 50h milling time respectively.

Table 4.3: Variation of coercive field (H_c), saturation (M_S) and remanent (M_R) magnetization with measuring temperature (T) for $CdFe_2O_4$ oxides.

	0h			50h		
T (K)	H_C (Oe)	M_S (emu/g)	M_R (emu/g)	H_c (Oe))	M_S (emu/g)	M_R (emu/g)
	± 0.3	±0.02	± 0.1	±0.03	±0.04	±0.2
300	38.2	0.58	36.0	8.55	12.70	8.6
200	38.9	0.79	32.9	17.48	23.57	17.2
150	39.2	1.03	59.5	23.76	27.47	19.0
100	66.5	1.31	119.6	40.85	31.09	76.8
50	68.8	1.62	87.6	100.80	33.87	100.7
10	197.3	2.39	198.1	514.89	33.53	510.9

515 Oe at 10 K is observed for the 50 h milled sample. According to Kneller's law coercive fields varies with temperature as [55]

$$H_C = H_C(0)\left[1 - \left(\frac{T}{T_B}\right)^{1/2}\right], \tag{4.3.1}$$

where $H_C(0)$ is the coercive field at $T = 0$ K which can be estimated by extrapolating the H_C versus temperature curve towards the field axis and T_B is the superparamagnetic blocking temperature of the nanoparticles. Figure 4.6 shows a plot of H_C versus $T^{1/2}$. The solid lines are linear fits to the data. H_C varies with T according to Kneller's law for temperature ranging from 50 K t0 300 K. The differences in magnetization and coercive fields between the unmilled and 50 h milled samples are attributed to the different particle sizes. The values of magnetization shown in Table 4.3 were recorded at a field of 5 kOe. There was no indication of saturating magnetization in both the as prepared and 50 h milled samples. A very high field would be needed to saturate the magnetization. The zero field cooling (ZFC) and field cooling

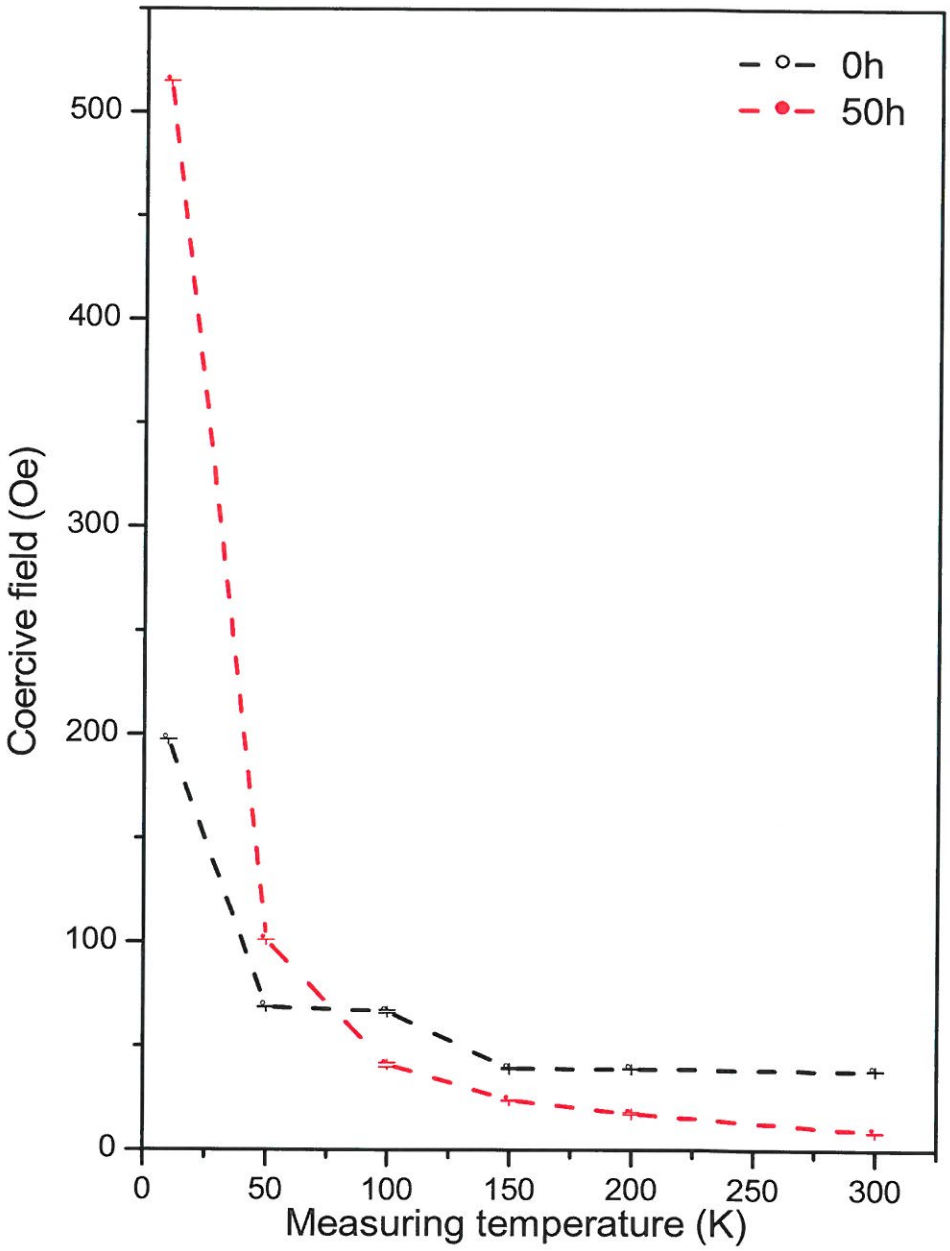

Figure 4.5: Variation of coercive fields as a function of temperature for as prepared (0 h) and 50 h milled $CdFe_2O_4$ oxides.

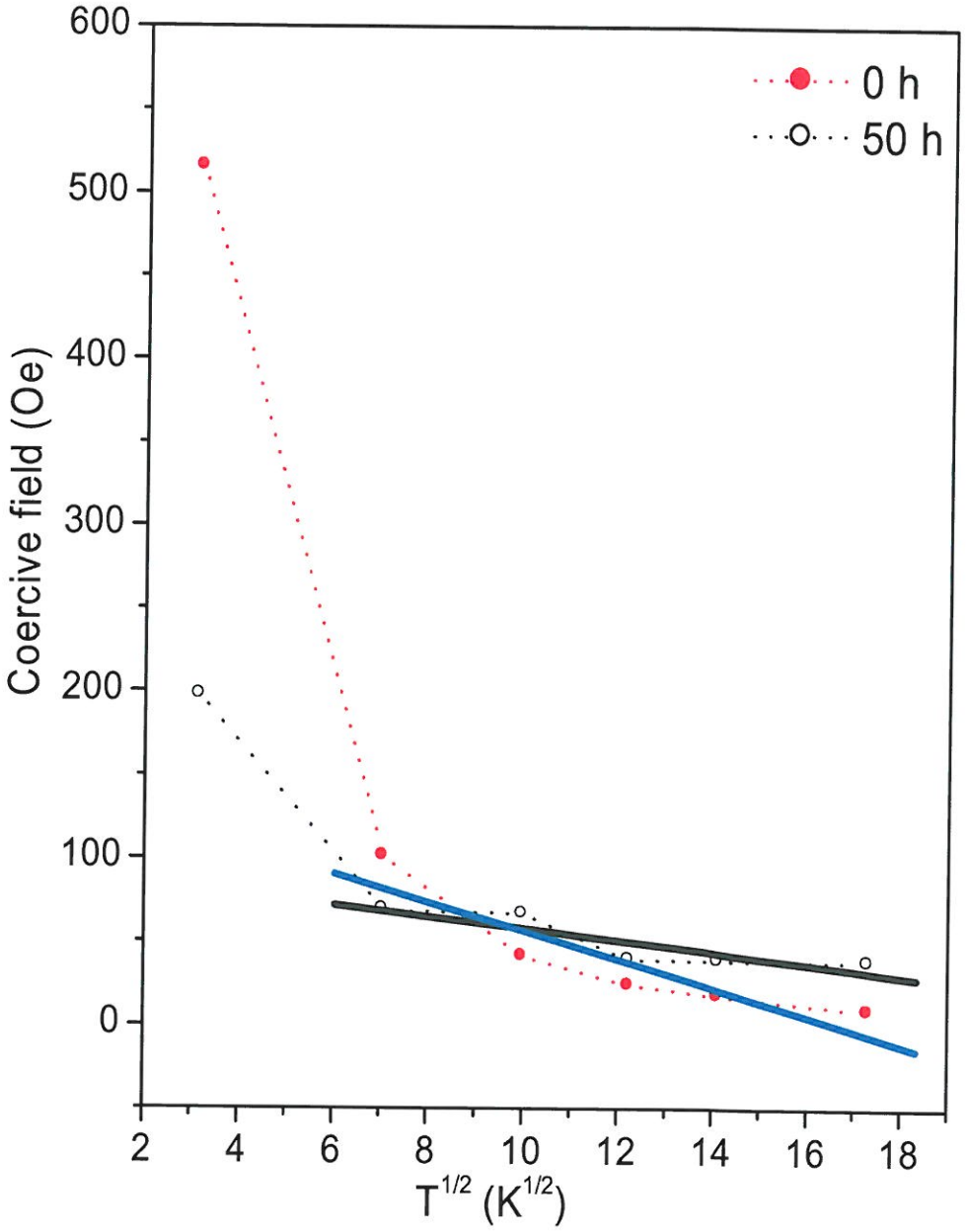

Figure 4.6: Variation of coercive fields as a function of $T^{1/2}$ for (0 h) and 50 h milled $CdFe_2O_4$ oxides.

(FC) (50 Oe) magnetization curves are shown in Figures 4.7 (a) and (b) for the as-prepared and 50 h milled compounds. During (FC), the oxides were cooled from 400 K to 10 K in the presence of an external magnetic field of 50 Oe. For ZFC measurements, the applied field of is zero during cooling to 10 K and the magnetization was recorded during warming up to 400 K in the presence of an external field for FC (50 Oe). FC magnetization of the as–prepared sample increases to a maximum at low temperature and then reduces rapidly with further reduction in temperature. The temperature dependence of the FC magnetization of the milled sample is different to that of the unmilled sample. FC magnetization of the 50 h milled compound increases to a maximum at 100 K and then reduces slowly and levels off with further reduction in temperature. The variations of ZFC magnetizations of the milled and unmilled samples are similar. The ZFC magnetization increases with reduction in temperature to a maximum and then decreases with further reduction in temperature. The drop in ZFC magnetization below the maximum blocking temperature is characteristic of re–entrant spin glass behavior [56]. The wide peaks observed in ZFC curves indicate wide distribution of particle sizes. Each particle with a particular size has a certain blocking temperature. The differences between the as–prepared and milled samples are associated with chemical disorder and reduced particle sizes due to milling.

4.4 Conclusions

The effect of grain size reduction on the magnetic properties of $CdFe_2O_4$ oxides has been investigated. High energy ball milling appears to affect the size of the particles. This is indicative of structural disorder induced by milling. Milling also appears to force some of Cd ions to transfer from A site to B site. This results in increasing magnetization in milled compounds. The Mössbauer results show the paramagnetic spin state in the $CdFe_2O_4$ oxides while the magnetizations show evidence of superparamagnetic bevavior induced by milling.

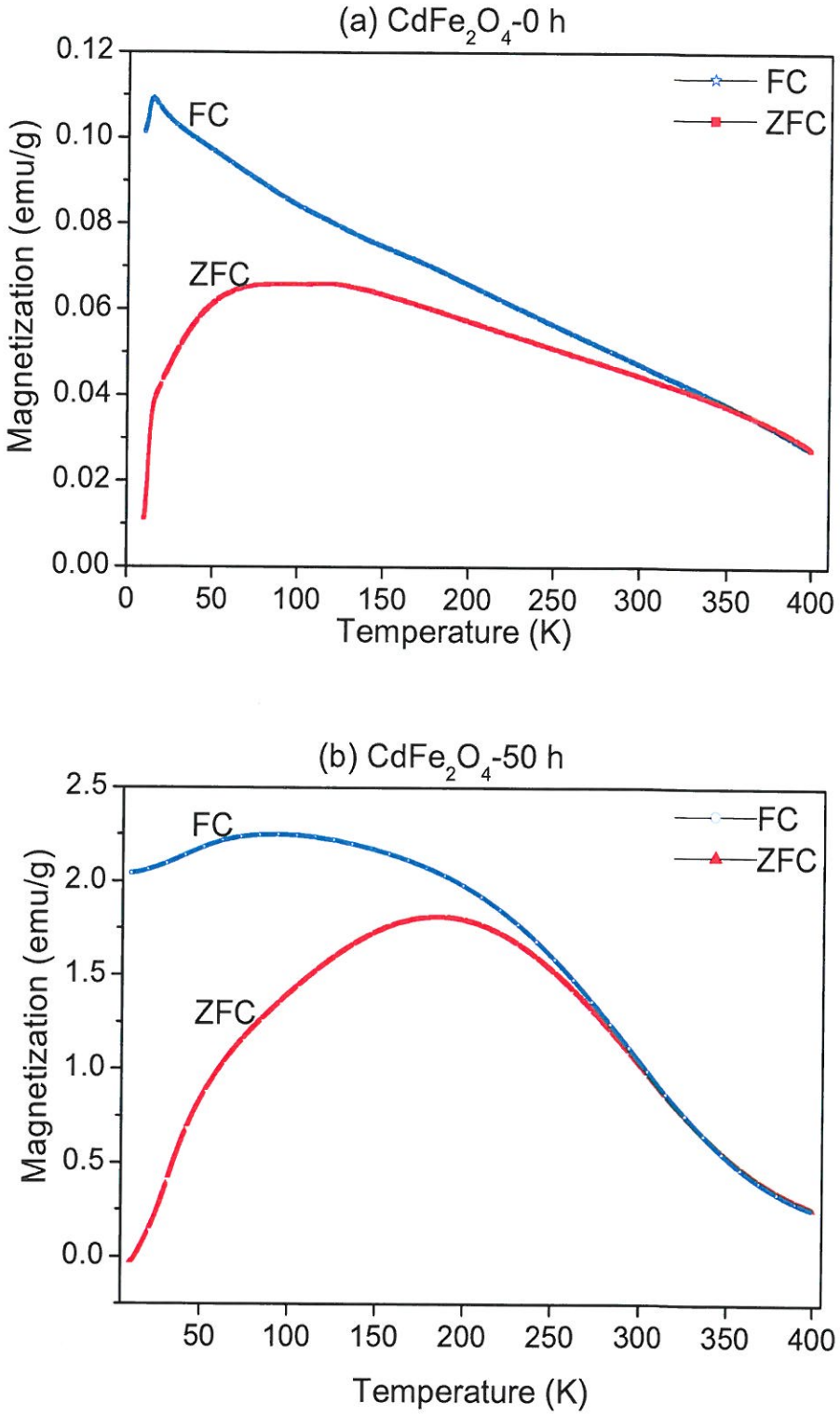

Figure 4.7: Variation of magnetization as a function of temperature for the (a) as–prepared (0 h) and (b) 50 hours milled samples.

Chapter 5

Magnetic properties of $Zn_{0.5}(Ni,\ Co)_{0.5}Fe_2O_4$ and $Zn_xMn_{1-x}Fe_2O_4$ oxides

Magnetic nanoparticles have broad practical applications in important technologies such as ferrofluids, magnetic drug delivery and high density information storage as discussed in chapter 1. The unusual properties of nanosized compared to bulk samples have attracted a lot of attention. The important features of magnetic nanoparticles are superparamagnetism and surface spins which can lead to a canted–spin structures. In the superparamagnetic state there are weak inter–particle magnetic interactions. Each nanoparticle has well defined magnetic order and behaves like a paramagnetic atom with a large magnetic moment and acts more or less independently. Super spin–glass behaviour can be observed where there is sufficiently strong magnetic interaction and the ensemble of nanoparticles show a collective behaviour. Efforts are still being made to improve synthesis techniques of nanophase ferrites. In this chapter we present the magnetic properties of $Zn_{0.5}Ni_{0.5}Fe_2O_4$, $Zn_{0.5}Co_{0.5}Fe_2O_4$ and $Zn_xMn_{1-x}Fe_2O_4$ nanosized ferrites synthesized by glycolthermal technique under low reaction temperature of 200 ^{0}C.

5.1 X–Ray diffraction results

The XRD data were used to confirm formation of cubic spinel phase of the compounds and to estimate crystallite sizes. The XRD spectra for $Zn_{0.5}Ni_{0.5}Fe_2O_4$ and $Zn_{0.5}Co_{0.5}Fe_2O_4$ compounds are shown in Figures 5.1 (a) and (b). The minor peak at $2\theta = 52^0$ not indexed in the XRD spectrum of the as prepared sample is attributed to an intermediate hematite α–Fe_2O_3 phase [58, 59]. This impurity phase disappears after annealing the as prepared sample between 500 ^{0}C and 600 ^{0}C. All the XRD peaks of the sample annealed at 600 ^{0}C are characteristic of single phase cubic spinel structure. The small impurity peak observed in the as prepared $Zn_{0.5}Ni_{0.5}Fe_2O_4$ oxide is not present in the as prepared $Zn_{0.5}Co_{0.5}Fe_2O_4$ oxide.

The variation of XRD partterns for $Zn_xMn_{1-x}Fe_2O_4$ as a function of Zn concentrations (x) is shown in Figure 5.2. All the XRD peaks were successfully indexed to pure cubic spinel structure. The broad peaks in some of the samples are indicative of fine particles. The grain sizes were calculated using the Debye-Scherrer formula as discussed in section 4.1. The average grain size for the as prepared $Zn_{0.5}Ni_{0.5}Fe_2O_4$ and $Zn_{0.5}Co_{0.5}Fe_2O_4$ oxides were 10.21±0.04 nm and 13.54±0.03 nm respectively. The values of gain sizes for the as prepared series of $Zn_xMn_{1-x}Fe_2O_4$ compounds are listed in Table 5.1. The particle size varies between 5 nm and 14 nm. The smallest particle size of 5.4 nm was obtained for the $Zn_{0.4}Mn_{0.6}Fe_2O_4$ sample ($x = 0.4$).

We have also investigated the effect of annealing time and annealing temperature on crystal size. The compound with the smallest particle size ($x = 0.4$) was divided into several specimens which were then annealed at 600 ^{0}C for 6 h, 18 h, 24 h, and 30 h. The XRD partterns for the $Zn_{0.4}Mn_{0.6}Fe_2O_4$ oxide annealed at different times are shown in Figure 5.3. The particle size of $Zn_{0.4}Mn_{0.6}Fe_2O_4$ increased from about 5.4 nm to 13.7 nm after annealing it for 6 h at 600 ^{0}C. The annealing temperature has significant effect on grain growth. As shown in Table 5.2, longer annealing times do not seem to signifi-

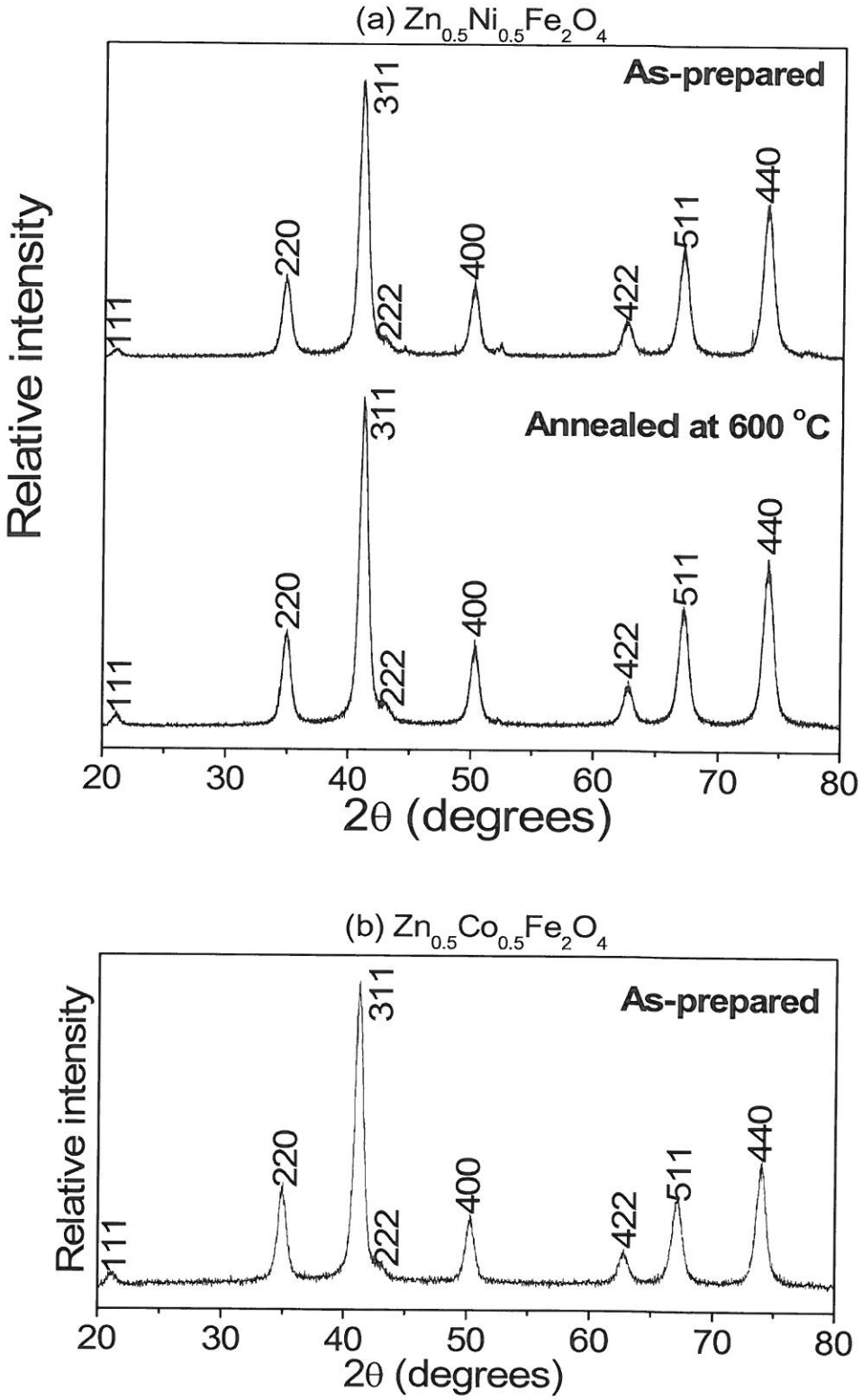

Figure 5.1: Variation of XRD patterns for $Zn_{0.5}(Ni, Co)_{0.5}Fe_2O_4$ oxides.

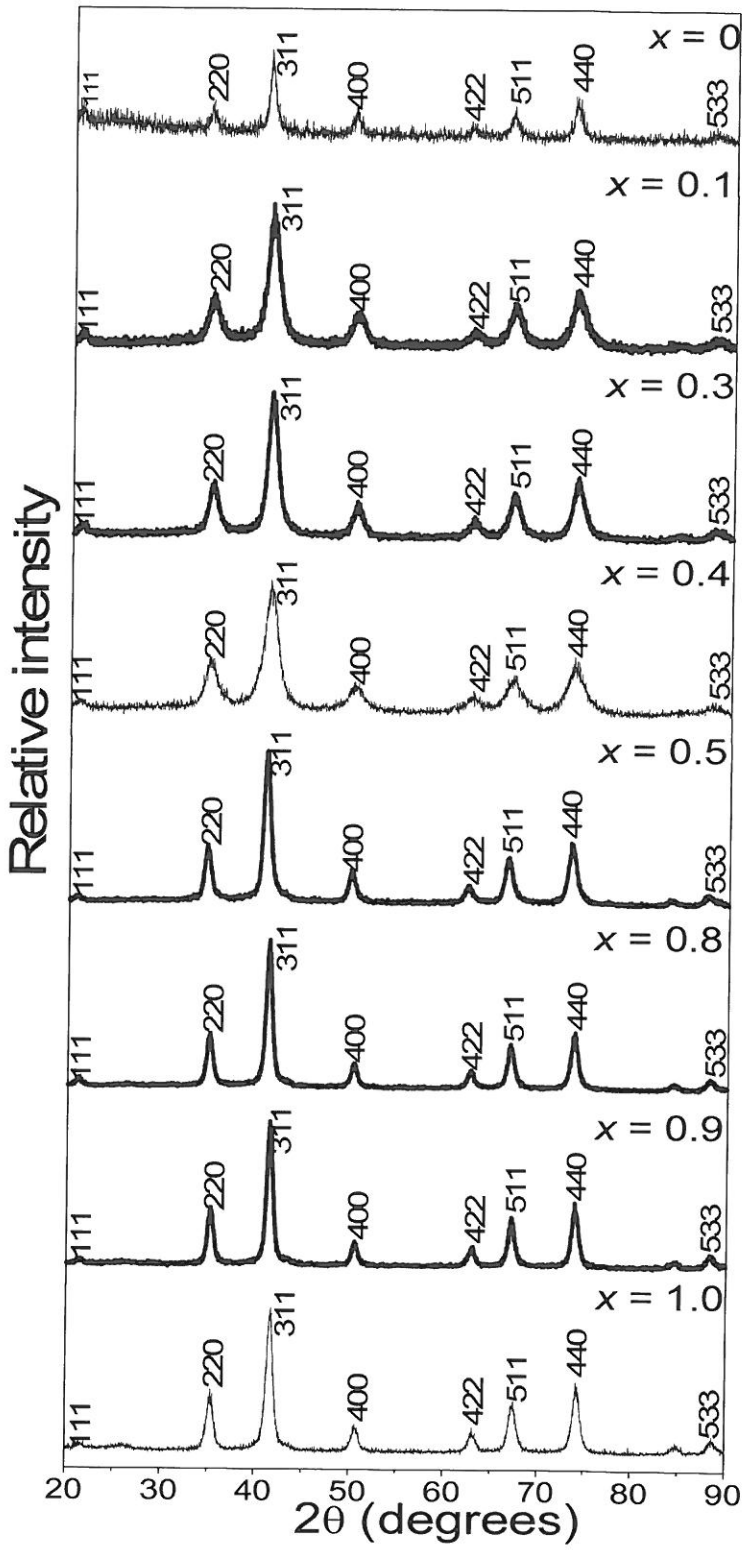

Figure 5.2: Variation of XRD patterns for $Zn_xMn_{1-x}Fe_2O_4$ with x.

Table 5.1: Variation of grain size (D), lattice parameter (a) and x-ray density (ρ_X) for $Zn_xMn_{1-x}Fe_2O_4$ as a function of x.

x	D (nm)	a (Å)	ρ_X(g/m^3)
	± 0.02	± 0.01	± 0.01
0	13.81	8.53	4.94
0.1	8.20	8.47	5.07
0.3	7.65	8.45	5.15
0.4	5.42	8.45	5.17
0.5	11.99	8.49	5.11
0.6	11.26	8.49	5.13
0.7	14.08	8.47	5.20
0.8	13.48	8.42	5.32
0.9	13.48	8.38	5.42
1.0	8.59	8.35	5.50

cantly affect particle sizes further. This is unlike the previous results reported by K. Maaz et al [55] where the particle size of $CoFe_2O_4$ were found to increase with annealing time.

The values of lattice parameters for $Zn_xMn_{1-x}Fe_2O_4$ deduced from XRD data are also presented in Table 5.1 and plotted in Figure 5.4. A non-linear variation of lattice constant with increasing x is observed. The lattice constant reduces to a minimum at about $x = 0.3$ and attains maximum at $x = 0.6$. A decrease in the lattice parameter with further substitution of Zn atoms occurs. The reduction of the unit cell parameter with increasing Zn content can be explained by substitution of bigger Mn^{2+} ions (0.91 Å) by smaller Zn^{2+} (0.74 Å) ions. The reduction in the lattice constants with increasing Zn constants was also observed in $Zn_xMn_{1-x}Fe_2O_4$ compounds produced by high

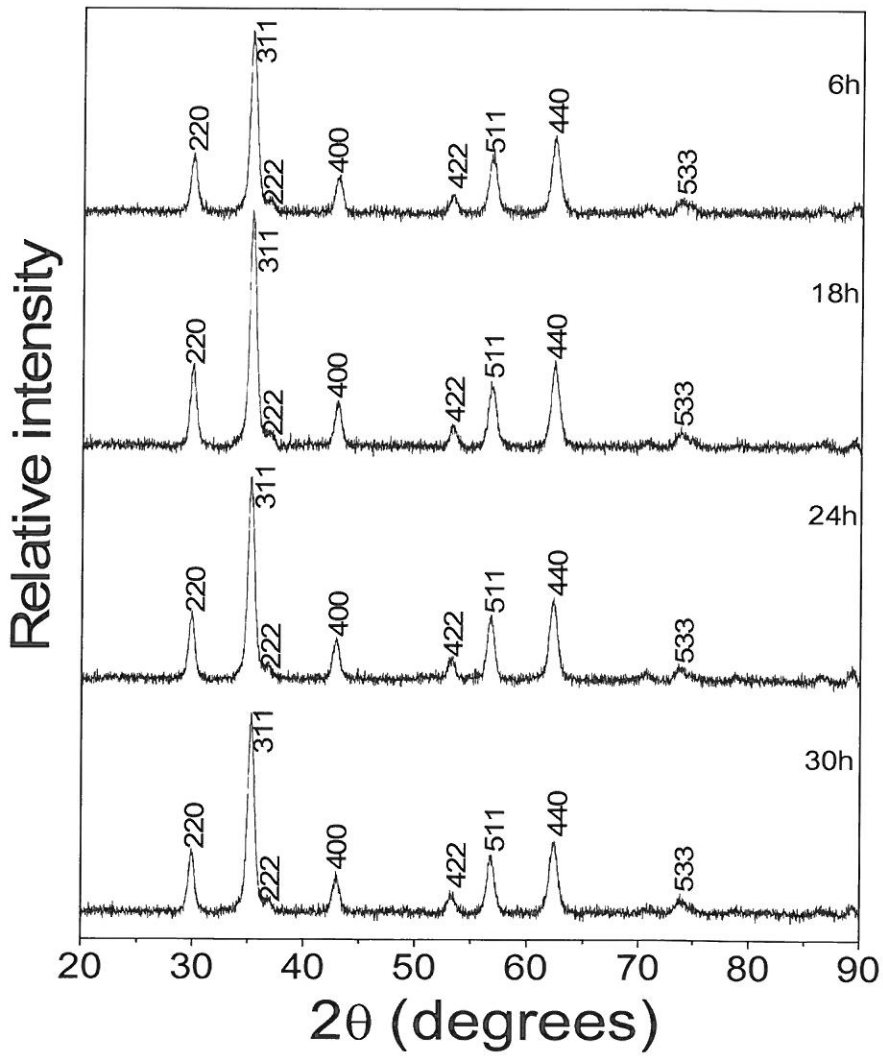

Figure 5.3: Variation of XRD spectra for $Zn_{0.4}Mn_{0.6}Fe_2O_4$ (annealed at 600 ^{0}C) with annealing time.

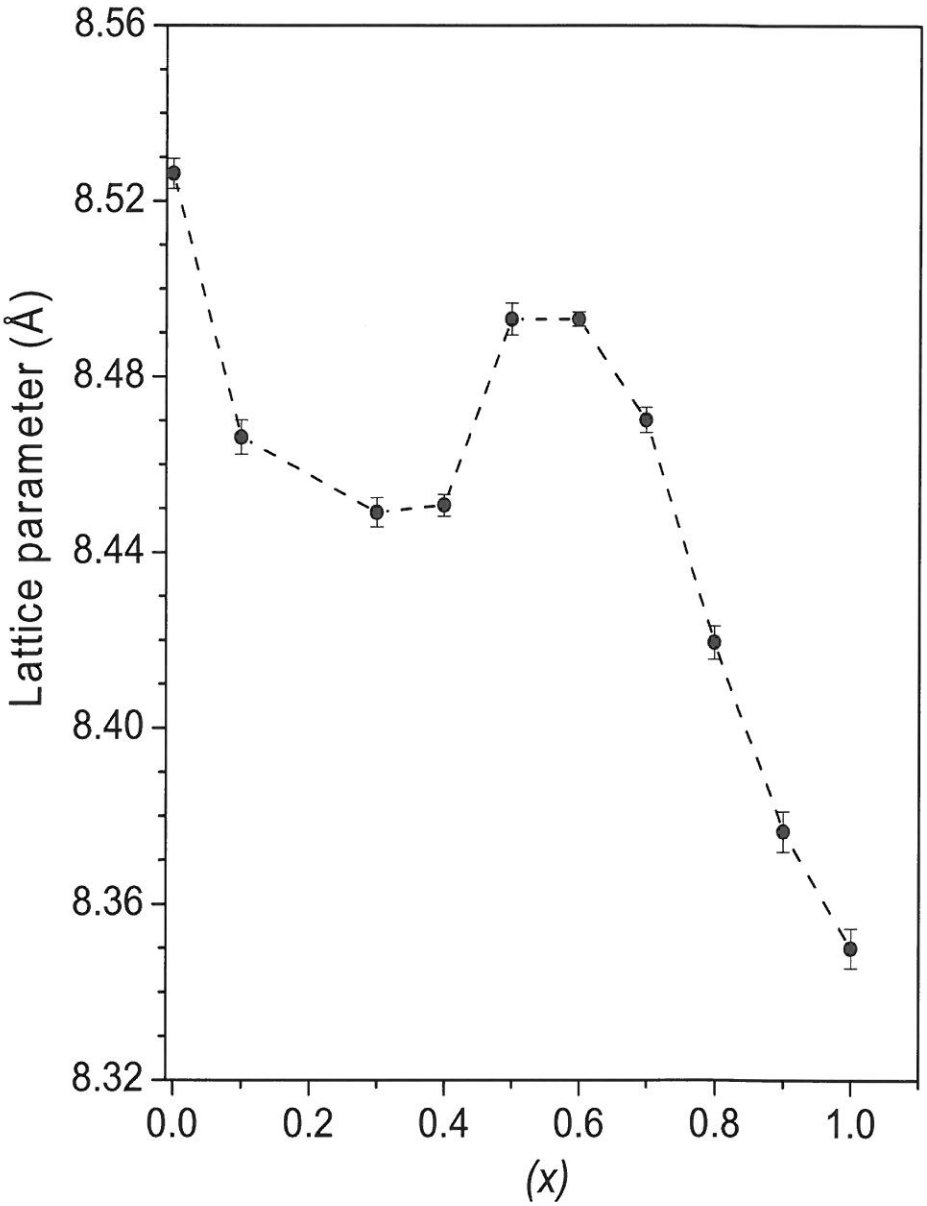

Figure 5.4: Variation of lattice parameter for $Zn_xMn_{1-x}Fe_2O_4$ oxides as a function of x.

Table 5.2: Variation of grain size (D), lattice parameter (a) and x-ray density (ρ_X) with annealing time (t) for $Zn_{0.4}Mn_{0.6}Fe_2O_4$ oxides annealed at 600 ^{0}C.

t (h)	D (nm)	a (Å)	ρ_X (g/m^3)
	$\pm$ 0.02	$\pm$ 0.01	$\pm$ 0.01
0	5.42	8.45	5.17
6	13.74	8.43	5.19
18	14.18	8.43	5.20
24	14.15	8.44	5.17
30	13.72	8.43	5.21

energy ball milling [11]. The increase in the lattice constants with increasing Zn concentration from about $x = 0.4$ to $x = 0.7$ which are observed in our samples may be due to the replacement of smaller Fe^{3+} (0.67 Å) by larger size Zn^{2+} (0.74 Å) at tetrahedral (A) sites. The complex variation of a with x observed in this work is similar to the changes in lattice constants observed in bulk $Zn_xMn_{1-x}Fe_2O_4$ produced by solid state reaction and then sintered at 1200 ^{0}C and 1300 ^{0}C [1]. The values of x–ray densities listed in Table 5.1 are also comparable to those of similar compounds [3].

5.2 Mössbauer spectroscopy results

Figure 5.6 shows the Mössbauer spectra of the as prepared $Zn_xMn_{1-x}Fe_2O_4$ oxides. The spectra could be resolved into two quadrupole doublets. This indicates paramagnetic spin state of Zn–based compounds. The data of isomer shifts, quadrupole splitting, line widths and Fe fractions at A and B sites deduced from the best fits to the experimental data are shown in Table 5.4. There is no significant change in isomer shift with increasing x. This indicates

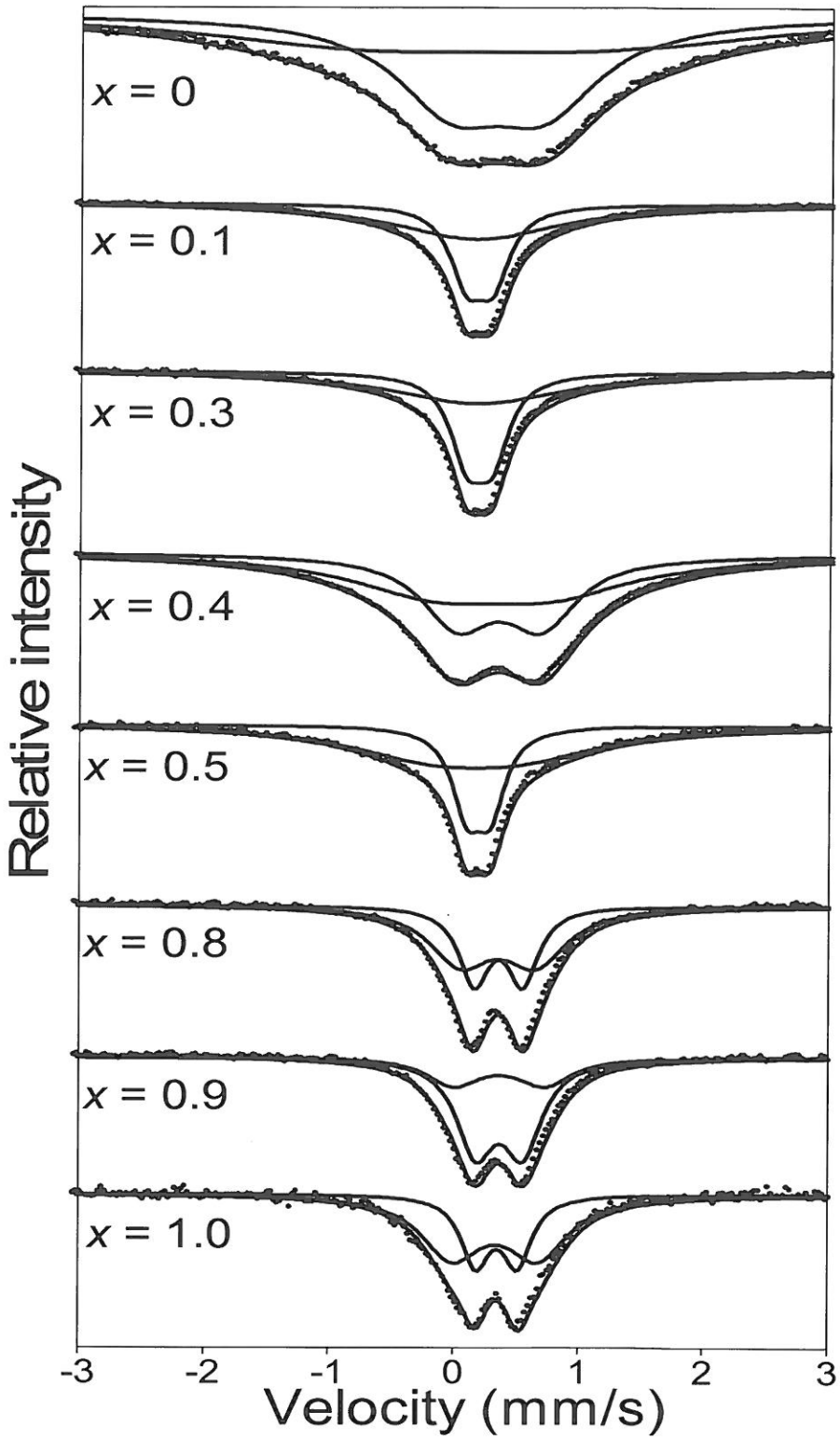

Figure 5.5: Variation of Mössbauer spectra for $Zn_xMn_{1-x}Fe_2O_4$ as a function of x.

Table 5.3: Variation of isomer shift (δ), quadrupole splitting (ε), line width (l) and Fe fraction (f) at A and B sites of $Zn_xMn_{1-x}Fe_2O_4$ as a function of x.

	δ (mm/s)		ε(mm/s)		l(mm/s)		f(%)	
x	δ_A	δ_B	ε_A	ε_B	l_A	l_B	f_A	f_B
	$\pm$ 0.01	$\pm$ 0.005	$\pm$0.02	$\pm$ 0.02	$\pm$0.03	$\pm$ 0.02	$\pm$0.6	$\pm$0.4
0	0.34	0.24	0.75	1.97	0.56	1.56	53.0	47.0
0.1	0.18	0.194	0.03	0.21	0.81	0.16	56.4	43.6
0.3	0.18	0.196	0.01	0.20	0.84	0.16	52.1	47.8
0.4	0.30	0.362	0.96	0.68	0.81	0.35	55.0	45.5
0.5	0.20	0.176	0.19	0.74	0.14	0.78	34.9	65.2
0.6	0.36	0.363	0.54	0.93	0.21	0.85	25.6	74.4
0.7	0.36	0.355	0.05	0.50	0.18	0.25	48.1	51.9
0.8	0.37	0.361	0.39	0.68	0.15	0.31	40.4	59.6
0.9	0.37	0.374	0.378	0.73	0.19	0.26	30.4	69.6
1.0	0.35	0.339	0.33	0.69	0.14	0.30	34.5	65.5

that the s electron charge distribution of the Fe ions is weakly affected by Zn concentration. The A site quadrupole splitting and line width are generally lower compared B sites. This behaviour is similar to the previous results of similar compounds [54] and is due to high symmetry at A site. The doublet areas indicating the Fe fractions at A and B sites are shown in Table 5.4. The variation of Fe fractions at A and B sites can be explained on the basis of the unstable distribution of Zn atoms between tetrahedral (A) and octahedral (B) sites as indicated by XRD results. A general increase of Fe component at B site or a decrease of Fe fraction at B site occurs. This can be explained by A site preference of Zn ions. Zn atoms tend to force Fe ions out of A sites.

5.3 Magnetization measurements

The hysteresis curves for $Zn_{0.5}(Ni, Co)_{0.5}Fe_2O_4$ oxides are shown in Figures 5.7 (a) and (b). No saturation was observed even in the presence of the magnetic field of fields up to 40 kOe. Higher magnetic fields are required to saturate magnetization. An increase in magnetization with decreasing sample measuring temperature occurs. This is associated with reducing thermal energies of the magnetic moments. The coercive fields reduce with increasing temperature as shown in Figure 5.8. A larger increase in H_c at low temperature for Zn substituted Co–ferrite compared to Zn substituted Ni–ferrite occurs.

The field cooled (FC) and zero field cooled (ZFC) magnetizations for Zn–Ni and Zn–Co compounds are compared in Figures 5.9 (a) and (b). During FC operation, the specimens were cooled from 380 K to 4 K in the presence of an external magnetic field of 100 Oe. For ZFC measurements the applied field to the sample was zero during cooling to 4 K and the magnetization was recorded during warming up to 380 K in the presence of the same external field of 100 Oe. The changes in magnetization for Zn–Ni and Zn–Co oxides are closely related. Reducing magnetization with increasing temperature during FC states is due to increasing thermal energies causing disordering of magnetic moments. A

continuous increase in ZFC magnetization with increasing temperature occurs for Zn–Ni oxide. For the Zn–Co oxide ZFC magnetization initially increase slowly with increasing temperature up to about 125 K. A rapid increase in magnetization with further increase in temperature occurs. The initial slow increase in magnetization at low temperatures may be due to the frozen magnetic moments. The ZFC magnetization attains a maximum and then drops to zero at the magnetic transition temperature. The temperature at which ZFC magnetization is maximum is called the blocking temperature of magnetic domains. Above the blocking temperature the magnetic domains are unblocked or are unconstrained. For the $Zn_{0.5}(Ni, Co)_{0.5}Fe_2O_4$ compounds the blocking temperature is above 400 K. The variation and magnitude of ZFC magnetization with temperature below the blocking temperature is associated with the corresponding magnitude or temperature dependence of coercive fields. The large decrease in coercive fields with increasing temperature (shown in Figure 5.8) is related to the change in ZFC magnetization below the blocking temperature. The coercive field is a measure of magnetocrystaline anisotropy. The large coercive fields and high magnetizations observed at low temperatures are due to magnetic anisotropy inhibiting alignment of magnetic moment in the magnetic field direction [28, 30].

FC and ZFC magnetizations of the as prepared and annealed $Zn_{0.4}Mn_{0.6}Fe_2O_4$ samples (at 600 ^{0}C for 6 hours) are shown in Figure 5.10. Some differences in the magnetizations for the as-prepared sample (with particle size of about 5.4 nm) and the annealed sample (with particle size of 13.7 nm) are observed. There is a discontinuity in the ZFC magnetization around 40 K in the as-prepared sample which becomes less significant after annealing. Two maxima are observed in the FC magnetizations which we suspect to be due to both antiferromagnetic and ferromagnetic phases. Higher magnetization is obtained in the annealed sample. The annealed hsample has higher magnetization which we associate with larger ferromagnetic grains. The typical hysteresis loop is shown in Figure 5.11 for the as prepared $Zn_{0.4}Mn_{0.6}Fe_2O_4$ oxide.

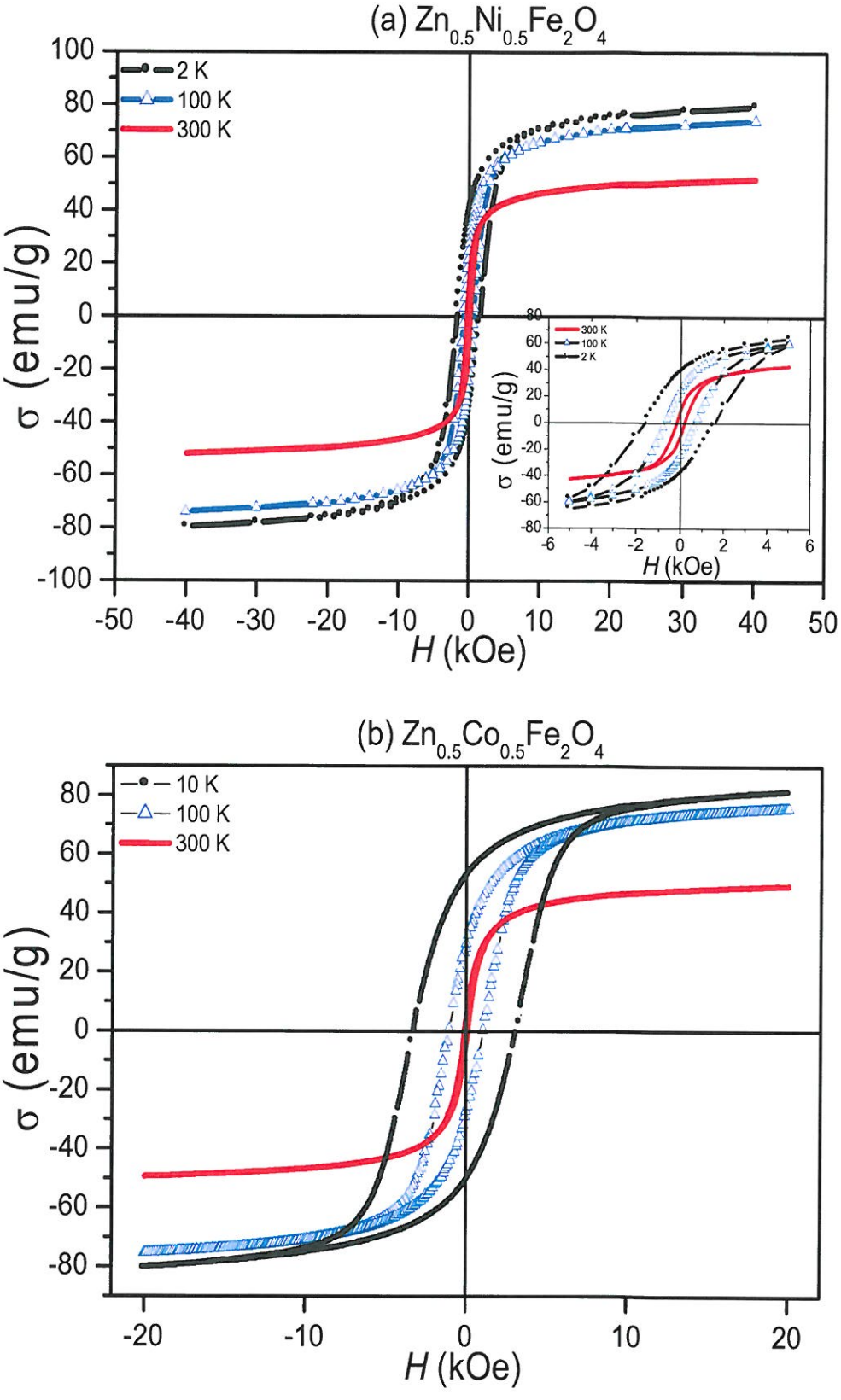

Figure 5.6: Variation of magnetization curves for (a) $Zn_{0.5}Ni_{0.5}Fe_2O_4$ ans (b) $Zn_{0.5}Co_{0.5}Fe_2O_4$ oxides with measuring temperature.

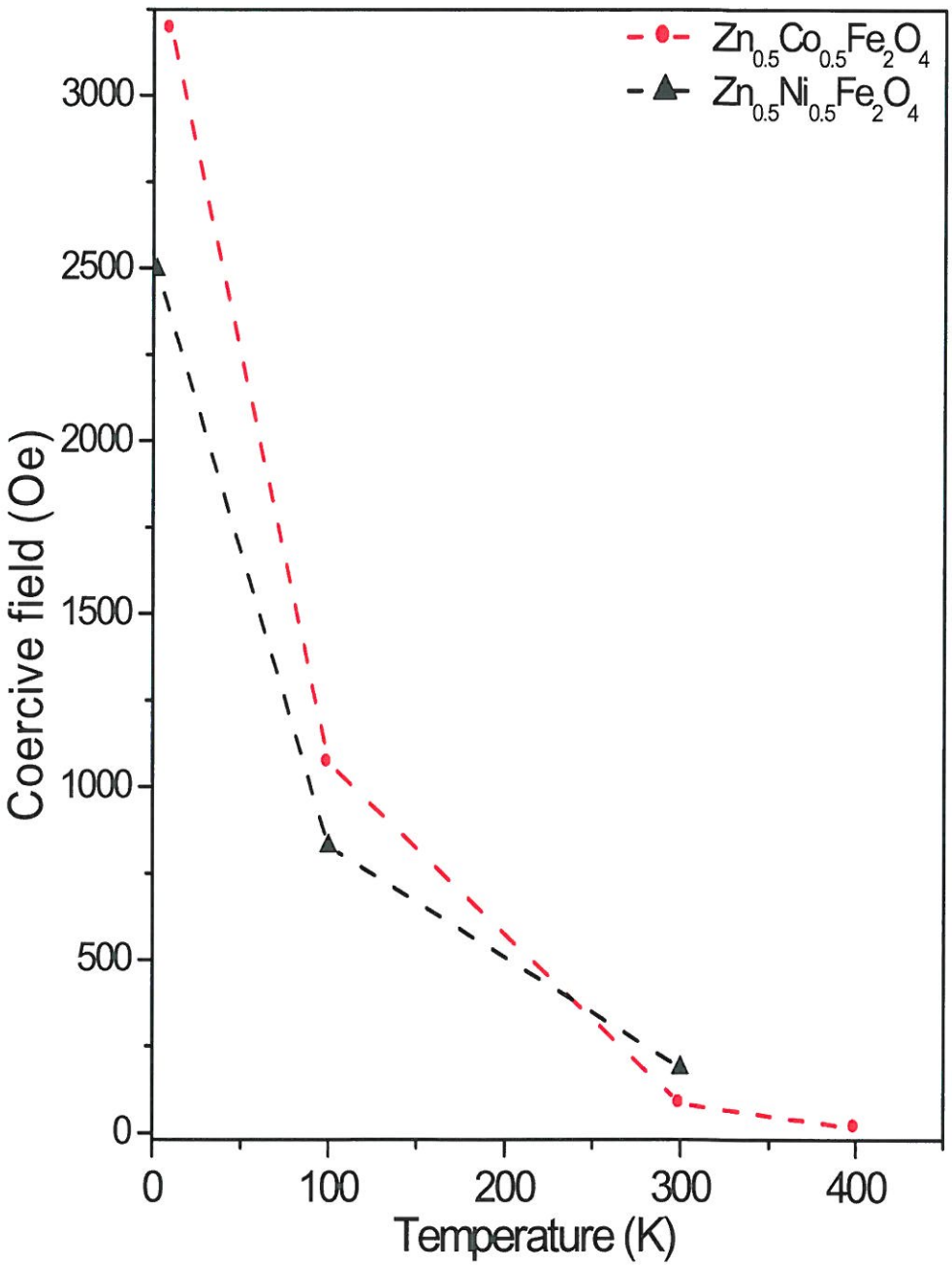

Figure 5.7: Variation of coercive fields for $Zn_{0.5}(Ni, Co)_{0.5}Fe_2O_4$ oxides with measuring temperature.

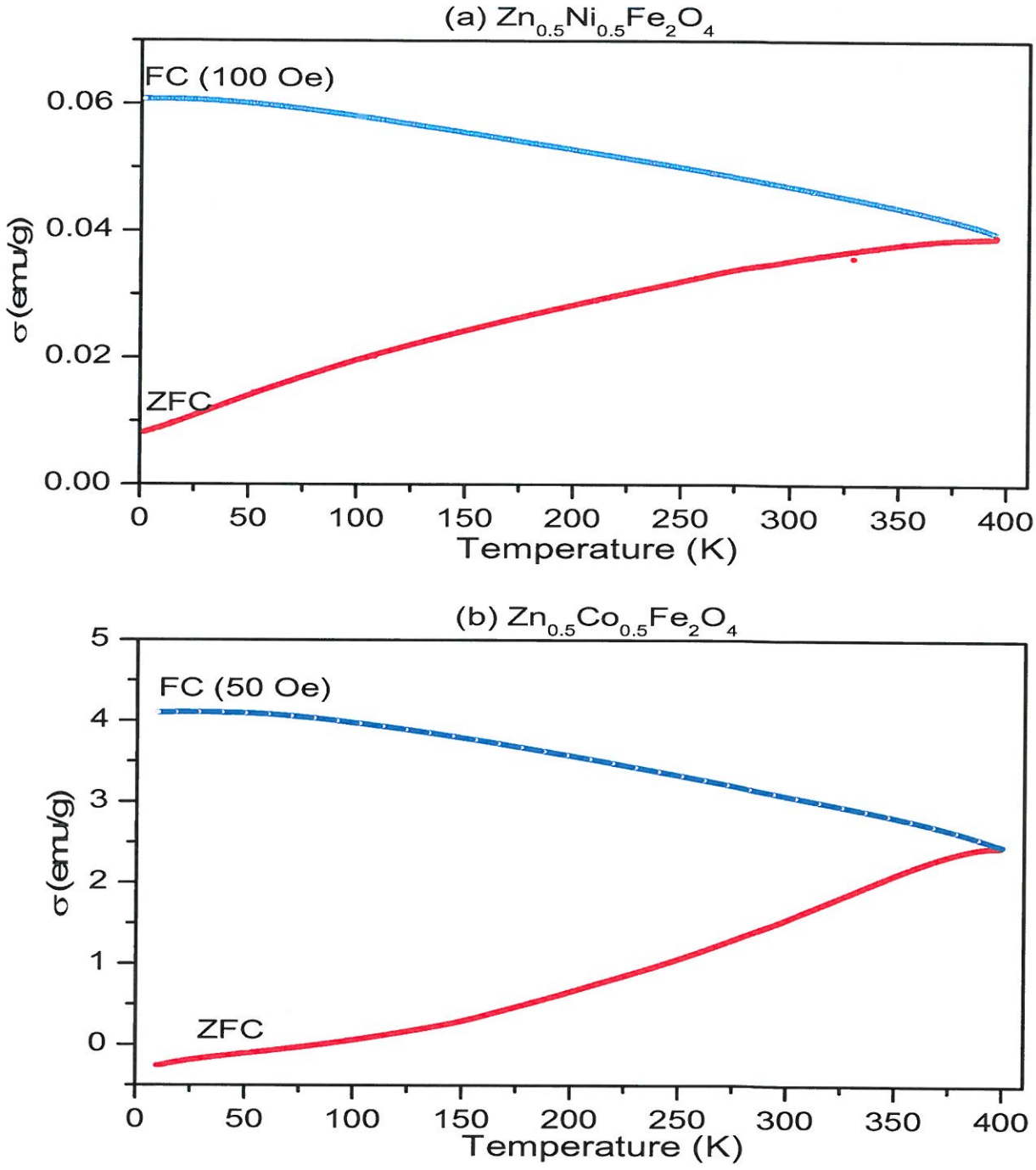

Figure 5.8: Variation of magnetization as a function of temperature for $Zn_{0.5}(Ni, Co)_{0.5}Fe_2O_4$ oxides.

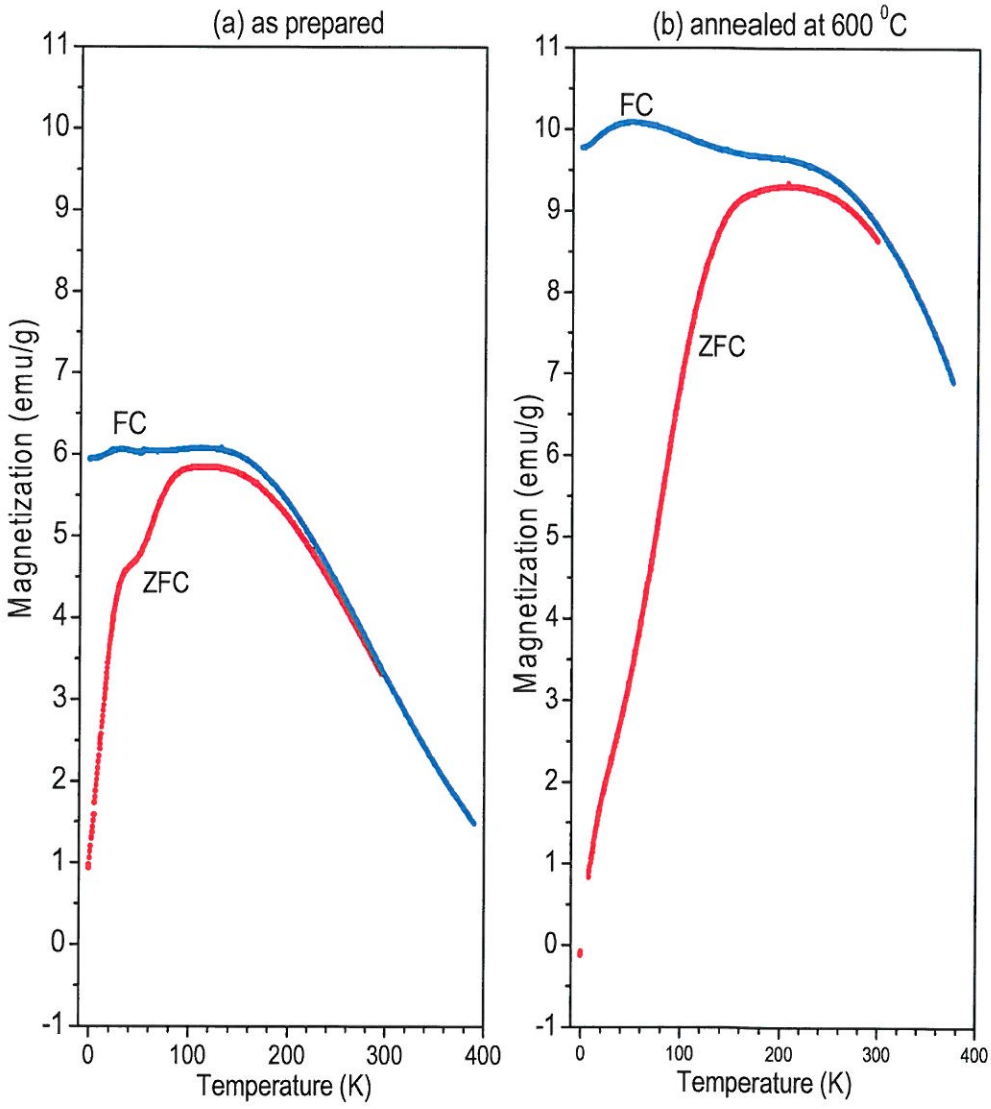

Figure 5.9: Variation of magnetization as a function of temperature for (a) raw and (b) annealed $Zn_{0.4}Mn_{0.6}Fe_2O_4$ oxides.

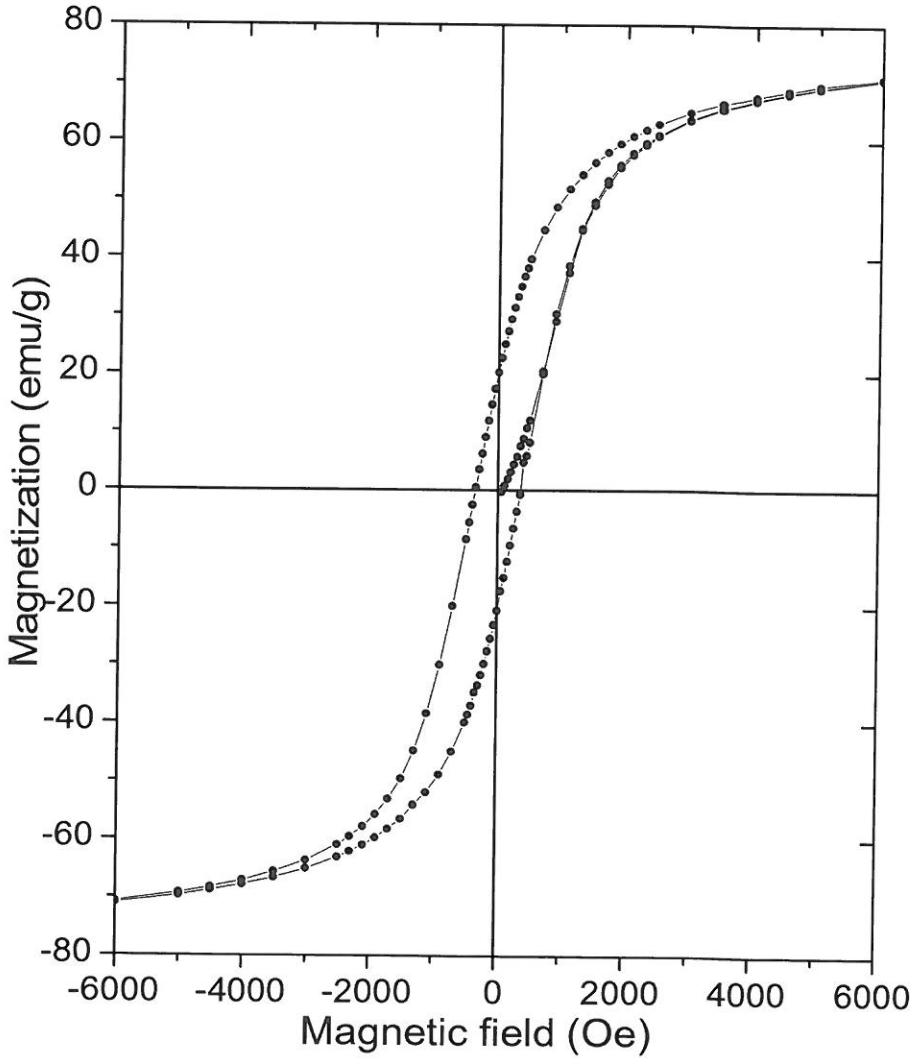

Figure 5.10: The hysteresis loop for raw $Zn_{0.4}Mn_{0.6}Fe_2O_4$ oxide.

5.4 Conclusions

The $Zn_{0.5}(Ni,\ Co)_{0.5}Fe_2O_4$ and $Zn_xMn_{1-x}Fe_2O_4$ nano–sized compounds with particle size ranging from 5 nm to 14 nm have been successfully synthesized and studied. A non–linear variation of lattice constants of $Zn_xMn_{1-x}Fe_2O_4$ with Zn content has been observed. The annealing time did not have a significant effect on the particle growth unlike the effect of the annealing temperature. We have found a discontinuity in the temperature dependence of magnetization which suggests more than one magnetic phase in both as–prepared and annealed $Zn_{0.4}Mn_{0.6}Fe_2O_4$ samples. The annealed sample has higher magnetization.

Chapter 6

Conclusions

Fine powders of $CdFe_2O_4$, $Zn_xMn_{1-x}Fe_2O_4$ and $Zn_{0.5}(Ni,\ Co)_{0.5}Fe_2O_4$ ferrites with particle size ranging from about 5 nm to 15 nm have been successfully produced by high energy ball milling and glycolthermal reaction.

The effects of milling on the structural and magnetic properties of $CdFe_2O_4$ have been investigated. High energy ball milling appears to have significant effects on properties. The reduction of lattice parameters with milling has been associated with structural defects caused by milling. This relates well with the broadening of the Mössbauer peaks with milling. An initial sharp decrease in grain size with milling time has been observed. The slow decrease of grain sizes after milling beyond 20 hours is associated with the particle size reaching atomic scale. The magnetic behavior observed in a 50 hour milled sample is associated with reentrant spin glass behavior. A general increase in magnetization with increasing milling time occurs. This has been attributed to inversion, i.e., redistribution of Cd atoms in both tetrahedral (A) and octahedral (B) sites. High energy ball milling appears to force Cd atoms from A to B sites. There was no significant change in corecive fields with reducing grain size observed. The oercive fields vary with temperature according to Kneller's law [55].

The system of $Zn_xMn_{1-x}Fe_2O_4$ nano ferrites were produced by glycolthermal reaction under same the conditions. All the Zn–based sample crystallized

with single phase cubic spinel structure. A non–linear variation of lattice constants of $Zn_xMn_{1-x}Fe_2O_4$ compounds as a function of x occurs. This has been explained on the basis of atoms involved and their redistribution amongst the interstitial sites. The sample $Zn_{0.4}Mn_{0.6}Fe_2O_4$ ($x = 0.4$) was found to have the smallest grain size of about 5.42 nm. We have observed anomalous magnetic behavior which seems to be grain size dependant for this compound.

The present study has provided us with useful information on the synthesis, structural and magnetic properties of spinel oxides. The work was presented at the 3^{rd} International Conference on Superconductivity and Magnetism (29 April–4 May 2012, Istabul, Turkey). We have also submitted two papers for publication [76, 77].

Bibliography

[1] M. M. Hessien, M. M. Radhad, K. El-Barawy, I. A. Ibrahim, J. Magn. Magn. Mater. 320 (2008) 1615.

[2] J. R. Hook, H. E. Hall, *Solid State Physics*, Second Edition, John Wesly & Sons Ltd, England, 1991, p. 1–19, 229–233.

[3] J. Z. Msomi, T. Moyo, T.B Doyle, J. Magn. Magn. Mater. 310 (2007) 2564.

[4] Y. Ying, T. W. Eom, Y. P. Lee, L. S. Ling, V. L. Mathe, J. Appl. Phys. 108 (2010) 023911.

[5] F.S. Li, H. Wang, L. Wang, J. Wang. J. Magn. Magn. Mater. 309 (2007) 295.

[6] C. N. Chinnasamy, A. Narayasanasamy, N. Ponpandian, K. Chattopdhyay, K. Shinoda, B. Jeyadevan, K. Tohji, K. Nakatsuka, T Furubayashi, I. Nakatani, Phys. Rev. B. 63, (2001) 184108.

[7] V. K. Mittal, P. chandramohan, S. Bera, M. P. Srinivasan, S. Velmurugan, S. V. Narasimhan, Solid state Commun. 137 (2006) 6.

[8] B. P. Rao, P. S. V. S. Rao, G. V. S. Murthy, K. H. Rao J. Magn. Magn. Mater. 268 (2004) 315.

[9] P. A. Shaikh, R. C. Kambale, A. V. Rao, Y. D. Kolekar, J. Alloys and Compd. 482 (2009) 276.

[10] O. Caltun, I. Dumitru, M. Fedel, N, Lupu, H. Chiriac. J. Magn. Magn. Mater. 320 (2008) e869.

[11] Z. G. Zheng, X. C. Zhong, Y. H. Zhang, H. Y. Yu, D. C. Zheng. J. Alloys Compd. 466 (2008) 377.

[12] R. A. Dunlap, A. Alghamdi, J. W. O. Brein, S. J. Penney, J. Alloys Compd. 365 (2006) 84.

[13] S. Dasgupta, K.B. Kim, J. Eckert, I Mnna, J. Alloys Compd. 424 (2006) 13.

[14] G. F. Goya, H. R. Rechenberg, J. Magn. Magn. Mater. 196–197 (1999) 191.

[15] F. S. Li, L. Wang, J. B. Wang, Q. B. Zhou, X. Z. Zhou, H. P. Kunkel, J. Magn. Magn. Mater. 286 (2004) 332.

[16] H. M. I. Abdallah, T. Moyo, J. Z. Msomi, J. Supercond Nov Mgan, 24 (2011)669.

[17] Q. Zeng, Y. F. Xiao, S. Z. Dong, X. B. Qiu, Z. Y. Zheng, R. Wang, J. Magn. Magn. Mater. 192 (1999) 321.

[18] Y. Xuan, Q. Li, G. Yang, J. Magn. Magn. Mater. 312 (2007) 464.

[19] C. Rath, K. K. Sahu, S. Anand, S. K Date, N. C. Mishra. R. P. Das: J. Magn. Magn. Mater. 202 (1999) 77.

[20] B. Jeyadevan, K. Tohji, K. Nakatsuka, A. Narayanasamy, J. Magn. Magn. Mater. 217 (2000) 99.

[21] G. Vaidyanathan, S. Sendhilnathan, R. Arulmurugan, J. Magn. Magn. Mater. 313 (2007) 293.

[22] R. Y. Hong, J. H. Li, S. Z. Zhang, G. Q. Di, H. Z. Li, D. G Wei, J. Alloys Compd. 480 (2006) 947.

[23] H. E. Zhang, B.F. Zhang, G. F. Wang, X. H. Dong, Y. Gao, J. Magn. Magn. Mater. 312 (2007) 126.

[24] K. J. Kim, H. K. Kim, Y. R. Park, J. Y. Park, J. Magn. Magn. Mater. 304 (2006) e106.

[25] G. V. Duong, R. S. Turtelli, N. Hinh, D. V. Linh, M. Reissner, J. Magn. Magn. Mater. 307 (2006) 313.

[26] X. Qi, D. Wu, J. Magn. Magn. Mater. 308 (2007) 289.

[27] R. N. Panda, J. C. Shihb, T. S. Chin, J. Magn. Magn. Mater. 257 (2003) 79.

[28] J. M. D. Coey, *Magnetism and Magnetic Materials*, Cambridge University Press, New York, 2010, p.1–15, 439–441.

[29] H. M. I. Abdallah, T. Moyo, J. Z. Msomi: J. Supercond Nov Mgan. DOI 10.1007/s10948–011–1231–4.

[30] J. Stöhr, H. C. Siegmann, *Magnetism From Fundumentals to Nanoscale Dynamics*, Springer, New York, 2006, p. 61–72, 511–517.

[31] J.Z. Msomi, T. Moyo, J. Mag. Mag. Mat. 321 (2009) 1246.

[32] S. Bedanta, W. Kleemann, J. Phys. D: Appl. Phys. 42 (2009) 013001.

[33] K. Maaz, A. Mumtaz, S. K. Hasanain, A. Ceylan, J. Magn. Magn. Mater. 308 (2007) 289.

[34] M. Grigorova, H. J. Blythe, V. Blaskov, V. Rusanov, V. Petkov, V. Masheva, D. Nihtianova, L. M. Martinaz, J. S. Munoz, M. Mikhov, J. Magn. Magn. Mater. 183 (1998) 163.

[35] S. Roy, J. Ghose, J. Magn. Magn. Mater. 307 (2006) 32.

[36] P. Hu, J. H. Yang, H. Wang, J. Tian, S. Zang, X. Wang, A. A. Volinsky, J. Magn. Magn. Mater. 322 (2006) 173.

[37] A. K. M. A. Hossain, T. S. Biswas, S. T. Mahmud, T. Yanagida, H. Tanaka, T. Kawai, J. Magn. Magn. Mater. 321 (2009) 81.

[38] Q. Chen, A. J. Rondinone, B. C. Chakoumakos, Z. G. Zheng, J. Magn. Magn. Mater. 194 (1999) 1.

[39] Y. Muraoka, H. Tatoshi, T. Kawai, Solid state Commun. 120 (2001) 255.

[40] M. Mozaffiri, F. Ebraiami, S. Daneshfozon, J. Amighian: J. Alloys Compd. 449 (2008) 65.

[41] J. Moulin, Y. Champion, J. M. Grenèche, F. Mazayrat, J. Magn. Magn. Mater. 254–255 (2003) 538.

[42] H. M. I. Abdallah, J. Z. Msomi, T. Moyo, J. J. Dolo, A Lančok: J Supercond Nov Mgan. 203 (2011) 99.

[43] H. P. Myers, *Introdactory Solid State Physics, Second Edition*, Taylor & Francis Ltd, London, 1985, p. 493–500.

[44] G. Burns, *Solid State Physics*, Academic Press, London, 1985, p. 564-594, 599-603.

[45] T. C. Gibbs, *Principles of Mössbauer spectroscopy*, Chapman and Hall, London, 1976, p.1-19, 23-43, 159-180.

[46] D. Jiles, *Introduction to Magnetism and Magnetic Materials*, Chapman and Hall, London, 1991, p. 50–52.

[47] M. A. Omar, *Elementary Solid State Physics*, Addison–Wesley, USA and Canada, p. 34–37, 51–53, 617–623.

[48] B. D. Cullity, S. R. Stoch, *Elements of X-ray Diffraction*, 3rd edition, Printice–Hall, Inc. USA, 2001, p. 19–24, 95–96.

[49] C. Kittel, *Introduction to Solid State Physics* 7th edition, John Weley & Sons, Canada, 1996, p. 28-30.

[50] N. W Ashcroft, N. D Mermin, *Solid State Physics*, W. B. Saunders Company, USA , 1976, p. 65–81, 95–97.

[51] M. G. Naseri, E. B. Saion, H. A. Ahangar, M. Hashim, A. H. Shaari, J. Magn. Magn. Mater. 323 (2011) 1745.

[52] J. Z. Msomi, T. Moyo, H. M. I Abdallah: J. Supercond Nov Mgan. DOI 10.1007/s10948–011–1235–0.

[53] D. Ravinder, T. Alivelumanga, Mater. Lett. 49 (2001) 1.

[54] J. Z. Msomi, K. Bharuth-Ram, V. V. Naicker, T. Moyo, Hyperfine Interactions 158 (2004) 151.

[55] K. Maaz, M. Usman, S. Karim, A. Mumtaz, S. K. Hasanain, M. F. Bertino, J. App. Phys. 105 (2009) 113917.

[56] S. M. Konoplyuk, V. V. Kokorin, O. V. Kolomiets, A. E. Perekos, V. M. Nadutov, J. Magn. Magn. Mater. 323 (2011) 763.

[57] P. H. Linh, T. D. Thanh, N. C. Thuan, L. V. Hong, N. X. Phuc, Commun. Phys. 19 (2009) 19.

[58] J. Z. Msomi, T. Moyo, J.J. Dolo Hyperfine Interact (2010) DOI 10.1007/s10751–010–0197–0.

[59] R. Gimenes, M. R. Baldissera, M. R. A. da Silva, C. A. da Silveira, D. A. W. Soares, L. A. Perazolli, M. R. da Silva, M. A. Zaghete, Ceram. Int. 38 (2012) 741.

[60] A. C. F. M. Costa, E. Tortella, M. R. Morelli, R. H. G. A. Kimanami: J. Magn. Magn. Mater. 256 (2003) 174.

[61] J. Z. Msomi, T. Moyo, H.M.I Abdallah, A.M. Strydom, D.Britz: J. Supercond Nov Mgan, 24 (2011) 711.

[62] www.qdusa.com/products/mpms.html, 04/10/2011.

[63] J. Z. Msomi, T. Moyo, Hyperlink Interact 176 (2007) 93.

[64] M. H. Mahmoud, A. M. Abdallasa, H. H. Hamdeh, W. M. Hikalb, S. M. Taherb, J. C. Hob: J. Magn. Magn. Mater. 263 (2003) 269.

[65] M. Mozaffiri, J. Ammighian, J. Matter. Lett. 260 (2003) 244.

[66] M. U. Rana, T. Abbas. F. A. Khawaja: Matter. Lett. 52 (2003) 389.

[67] R. V. Mangalaraja, S. Ananthakumar, P. Mahohar and F. D. Gnanam: Mater. Lett. 57 (2003) 1151.

[68] S. H. Hong, J. H. Park, Y. H. Choa, J. Kim: J. Magn. Magn. Mater. 290–291 (2005) 1559.

[69] S. Yan, J Geng, L. Yin, E. Zhou: J. Magn. Magn. Mater. 277 (2004) 84-89.

[70] F. S. Wang , J. Li: J. Magn. Magn. Mater. 223 (2001) 223–230.

[71] J. Z. Msomi, T. Moyo, K. Bharuth-Ram, Hyperfine Interactions (C), 5 (2002) 181.

[72] J. Giria, T. Sriharshaa, S. Asthanaa, K. Tumkur, G. Raob, K. Arun, D. Bahadur: J. Magn. Magn. Mater. 293 (2005) 55.

[73] E. Kuzmann, K. Lazar(eds) ISIAME 2008. DOI:10.1007/978–3–642–01369–0–13.

[74] K. Mbela, T. Moyo, J. Z. Msomi: J. Supercond Nov Mgan. DOI 10.1007/s10948–011–1234–1.

[75] R. H. Kodama: J. Magn. Magn. Mater 200 (1999) 359–372.

[76] J.Z. Msomi, T.A. Nhlapo, T. Moyo, M. Öztürk, N. Akdoğan; Structural and magnetic changes induced by high energy ball milling in $CdFe_2O_4$ oxide, Journal of Super Cond. Nov. (submitted for publications, May 2012).

[77] J.Z. Msomi, T.A. Nhlapo, T. Moyo, J. Snyman, A.M. Strydom; Structural, Mössbauer and magnetic properties of $Zn_xMn_{1-x}Fe_2O_4$ nanoferrites, Journal of Super Cond. Nov. (submitted for publications, May 2012).